

**DEVELOPMENT OF A HIGH-THROUGHPUT MAGNETIC
CHARACTERIZATION TECHNIQUE AND ITS APPLICATION TO
PROCESS PARAMETER DEVELOPMENT FOR ELECTRON
BEAM POWDER BED FUSION OF PERMALLOY**

A Thesis
Presented to
The Academic Faculty

by

Stefan Colton

In Partial Fulfillment
of the Requirements for the Degree
Master of Science in the
George W. Woodruff School of Mechanical Engineering

Georgia Institute of Technology
December 2023

COPYRIGHT © 2023 BY STEFAN COLTON

**DEVELOPMENT OF A HIGH-THROUGHPUT MAGNETIC
CHARACTERIZATION TECHNIQUE AND ITS APPLICATION TO
PROCESS PARAMETER DEVELOPMENT FOR ELECTRON
BEAM POWDER BED FUSION OF PERMALLOY**

Approved by:

Dr. Aaron Stebner, Advisor
School of Mechanical Engineering
Georgia Institute of Technology

Dr. Surya Kalidindi
School of Mechanical Engineering
Georgia Institute of Technology

Dr. Christopher Saldaña
School of Mechanical Engineering
Georgia Institute of Technology

Dr. Alex Leary
Materials and Structures Division
NASA Glenn Research Center

Date Approved: August 7th, 2023

ACKNOWLEDGEMENTS

I would like to thank my advisor, Dr. Aaron Stebner, for his endless support and wisdom during my past two years here at Georgia Tech. Furthermore, I would like to recognize my labmates and all those working in the AMPF for their invaluable help and collaboration. I additionally owe this group for making Atlanta a second home to me.

I would also like to thank Sandia National Laboratories for funding this research under the Beyond Fingerprinting Lab Directed Research and Development (LDRD) program through contract #DE-NA0003525 and my many collaborators from Sandia who greatly supported and inspired this work. This includes Brad Boyce and the rest of the Beyond Fingerprinting team, as well as Andrew Kustas and Jesse Adamczyk who provided materials, knowledge, and ideas.

Finally, I would like to acknowledge my family. I am deeply grateful to my mother and father for everything they have done for me on the long journey to this point, including the incredible value they put on education. I would also like to give thanks to my partner, Aradhita, who has been an incredible pillar of support to me through this entire process.

TABLE OF CONTENTS

ACKNOWLEDGEMENTS	iv
LIST OF TABLES	vii
LIST OF FIGURES	viii
LIST OF SYMBOLS AND ABBREVIATIONS	xii
SUMMARY	xv
CHAPTER 1. Introduction	1
1.1 Motivation	1
1.2 Thesis Organization	6
CHAPTER 2. Background	7
2.1 Electromagnetism	7
2.2 Ferromagnetism	8
2.3 Shape Demagnetization Effect	10
2.1 Frequency Effects	11
2.2 Magnetic Characterization of Bulk Ferromagnetic Samples	11
2.2.1 Vibrating Sample Magnetometer (VSM)	13
2.2.2 Coercimeter	14
2.2.3 Alternating Gradient Magnetometers (AGM)	14
2.3 Electron Beam Powder Bed Fusion	14
2.4 Permalloy	16
2.5 Active Learning Approaches for Materials Research	16
CHAPTER 3. Novel Technique For The High-Throughput Characterization of Soft Magnets	18
3.1 Introduction	18
3.2 Materials and Methods	21
3.3 Theory and Design	23
3.3.1 Architecture Selection	23
3.3.2 Theory	24
3.3.3 Implementation	31
3.4 Results and Discussion	36
3.4.1 <i>J_{sat}</i> measurements accurate across wide range of values, approximately 1% relative errors when a using constant reference field	37
3.4.2 Coercivity repeatable to 20-30A/m, with greater accuracy. Shape biases minimal	38
3.4.3 Applicable to as-built AM specimens with poor form	40
3.4.4 Application to data-intensive measurements demonstrated	40
3.5 Conclusion	41

CHAPTER 4. Process Optimization of the Electron Beam Powder Bed Fusion of Permalloy	43
4.1 Introduction	43
4.2 Materials and Methods	45
4.2.1 Specimen Manufacture via Electron Beam Powder Bed Fusion	45
4.2.2 Characterization	51
4.2.3 Experimental Design	52
4.2.4 Active Learning	53
4.3 Results	56
4.3.1 Powder Characteristics	56
4.3.2 Printability	57
4.3.3 Surface Condition	59
4.3.4 Density	62
4.3.5 Mass Magnetization	64
4.3.6 Coercivity	65
4.3.7 Process Monitoring	66
4.3.8 Microscopy and Microstructure Characterization	67
4.4 Discussion	69
4.4.1 Sintered Powder can be Largely Broken Down	69
4.4.2 Surface Condition Highly Dependent on Four Factors Including “Quasi-Beam” Advanced Patterning Techniques	69
4.4.3 Density Highly Dependent on Energy Density, Power	71
4.4.4 Statistically Significant Relationships Between Energy Density and Mass Magnetization	73
4.4.5 Low Coercivity Driven by PBF-EB Thermal History	73
4.5 Conclusion	73
CHAPTER 5. Closing	75
5.1 Overall Conclusions	75
5.2 Limitations and Future Work	75
5.2.1 Magnetic Characterization	75
5.2.2 Electron Beam Powder Bed Fusion	77
APPENDIX A. High-Throughput Measurement of the Coefficient of Thermal Expansion of AM Samples	79
APPENDIX B. Details of Calculation of Magnetic Field From Permanent Magnet Positions	86
REFERENCES	88

LIST OF TABLES

Table 1	Maxwell's Equations of Classical Electromagnetism	7
Table 2	Comparison of magnetic characterization techniques on basis of high-throughput screening of bulk samples.	20
Table 3	Comparison of H_c, J_{sat} for different Fe-6Si Geometries (N=15, each)	39
Table 4	Repeatability of H_c, J_{sat} for 6 Similar AM Permalloy Specimens	40
Table 5	Measured Composition of Fe80Ni4Mo Powder, per Supplier	45
Table 6	Printer Characteristics	46
Table 7	Electron Beam Powder Bed Fusion Factors	50
Table 8	Electron Beam Powder Bed Fusion Co-factors	51
Table 9	Powder Size Distribution Percentiles	57
Table 10	First order effect test for least-squares regression of mass magnetization	64
Table 11	Fit results for Kovar specimen	84

LIST OF FIGURES

Figure 1	Representative hysteresis loop of a ferromagnetic material.	9
Figure 2	Shearing of hysteresis loop due to the shape demagnification effect. Blue - J vs. H_{eff} ; red - J vs. H_{ext}	11
Figure 3	Simplified representations of the most common operating principles for the characterization of bulk ferromagnetic samples.	12
Figure 4	Simplified schematic of a Vibrating Sample Magnetometer	13
Figure 5	Schematic of the PBF-EB Process. To avoid a “smoke-out” event, the plate is first heated by diffuse beam to a temperature which will lightly sinter the powder. The recoater sweeps powder from the powder piston to the build piston, which is then preheated by diffuse beam. A concentrated beam then scans the desired patterns, and the pistons actuate to enable another coating of powder.	15
Figure 6	The magnetic field H in the x-direction (dashed) and magnetic field gradient H_x between two opposing permanent magnets. Near the central axis these quantities will be relatively uniform over an area perpendicular to this axis.	25
Figure 7	Representative evolution of $H_{ext}(t)$. The solid lines represent a complete hysteresis loop.	25
Figure 8	Decomposition of the external field H_{ext} into a constant and graded component based on sample coordinated. It is assumed that the gradient in H_{ext} is constant over the length of the sample, equal to H_x	27
Figure 9	Demonstration of the effect of ξ , showing how it is constrained by the equal and opposite coercivity condition.	29
Figure 10	Physical realization of proposed instrument	32
Figure 11	a) Detail view of flexure and specimen mounting b) View of flexure, magnets from through-beam sensor. The deflection of the flexure is calculated, as well as the position of each magnet relative to the median of the flexure.	33
Figure 12	Actuation sequence of the permanent magnets, for a complete cycle	35
Figure 13	Actuation of the magnets vs. flexure deformation, typical response. Arrows indicate the locations of the sequence of images shown in	36

	Figure 12. Between the two positive peaks is one complete hysteresis loop	
Figure 14	Typical magnetic hysteresis loop measured by the proposed instrument, with high saturation and coercivity. The orange lines represents a constant H_{eff} at H_{ref} , used to estimate J_{sat} while compensating for shape demagnification effects.	36
Figure 15	Typical magnetic hysteresis loop measured by instrument with low saturation and low coercivity.	36
Figure 16	Error in J_{sat} measurements for graded Hiperco50/Hymu80 specimens compared to VSM. Two calculations of J_{sat} are shown: calculated as the maximum value of J at H_m , and at a common reference value H_{ref} of H_{eff}	37
Figure 17	Magnetic hysteresis loop for wrought Permalloy, with expected $H_c \approx 0$	39
Figure 18	First-Order Reversal Curve of AM specimen. The specimen had a full loop coercivity of approximately 3000 A/m.	41
Figure 19	The organization of build plate. Specimens designated for process optimization are arranged evenly in an annular region. These specimens are bounded on the inside and outside by a total of 6+ specimens designated for the purpose of process monitoring. Finally, two single-track line scans provide a set of coordinate axes for reference.	47
Figure 20	Architecture of break-off specimens. 10 layers are printed at an energy density of 0.8 J/mm² to ensure fusion to the build plate and accommodate any initial settling of the build plate. Subsequently, 25 layers are printed at energy density varying progressively from 0.4 J/mm² to 0.3 J/mm² . Finally, the 60 layers with the intended factors are printed. The melt pools from these can extend well into breakoff section, as can be seen above. Architecture of break-off specimens. 10 layers are printed at an energy density of 0.8 J/mm² to ensure fusion to the build plate and accommodate any initial settling of the build plate. Subsequently, 25 layers are printed at energy density varying progressively from 0.4 J/mm² to 0.3 J/mm² . Finally, the 60 layers with the intended factors are printed. The melt pools from these can extend well into breakoff section, as can be seen above.	48
Figure 21	Different scan strategies and their featurization. a) “Scan” can be either “line” or “dot,” as either a set of parallel lines or grid of point scans, respectively. “Hatch” determines the spacing of adjacent	49

lines/dots. b) Layer-to-layer “rotation” and layer spacing. c) “Step” determines order according to the gap between sequential lines/dots, effectively creating multiple passes.

Figure 22	Set power (orange) vs. actual power (blue). One can observe it takes approximately 5 seconds to achieve steady state when ramping up, and approximately 2 seconds when ramping down.	54
Figure 23	SEM image of as-received Permalloy Powder. Many particles are highly irregular, featuring a large aspect ratio or consisting of a conglomeration of smaller particles.	56
Figure 24	Powder Size Distribution, calculated from SEM image using circle equivalent diameter (N=174).	57
Figure 25	a-c) Progression of “smoke-out” event at 760°C. d) Nominal scanning at 850°C	58
Figure 26	Transient cooling from 850°C after a completed print	58
Figure 27	a) 3D measurement, from Keyence VR-3200. b) Picture of typical print, showing specimens with a variety of different surface conditions post-sandblasting.	59
Figure 28	Surface Roughness parity plot, utilizing Leave-One-Out Cross-Validation (LOOCV). GPR is clearly unable to model this response	60
Figure 29	Results from a single LHS print. Regardless of all other factors, a step size of 1 reduces surface roughness (Sa) growth with energy density	60
Figure 30	Surface roughness results, classified as poor/acceptable based on if the Sa surface roughness is greater than 250 μm . Convex regions are used to approximate the regions where poor surface condition is	61
Figure 31	Confusion matrix for classifying surface condition. The practicalities of avoiding recoater damage limited the number of true positives which could be sampled.	61
Figure 32	Cross Validation of GPR trained on Archimedes density. Some clustering of residuals can be visible, such as at the lower "tail" of overestimated densities. Overall, the residuals are well behaved and indicate a successful fit of the model. The clustering that is present can in part be explained by print-to-print variation.	62
Figure 33	Best predicted densities by GPR, along with individual data points. The other 4 factors have minimal impact on density. A clear trend	63

can be seen as Energy Density and to a lesser extent, power, increase density.

Figure 34	Change in density due to step = 3 vs. step = 0, for ED. It can be seen at higher energy densities, larger step has a slight negative impact on density.	63
Figure 35	Mass Magnetization increases with Energy density (N=102)	65
Figure 36	Distribution of measured coercivities from a single batch. No trends were found relating to the different factors.	65
Figure 37	Results of process monitoring, considering two major possible cofactors of build plate temperature and the number of breakoff layers. “Inside” references are located near the center of the build plate, and “outside” references with the opposite definition are distinguished. While there is clear print-to-print variation, there is no apparent dependency on either of these cofactors or on the chronology.	66
Figure 38	Cross section of specimen with ED of 9.5 J/mm ² and Power of 917W. While the center is nearly fully dense, some pores and cavities exist at the sides and bottom.	67
Figure 39	Cross section of specimen with ED of 4.9 J/mm ² and Power of 917W. While the center is nearly fully dense, large pores and cavities exist at the sides and bottom.	68
Figure 40	Cross section of specimen with ED of 3.0 J/mm ² and power of 917W. Significant porosity and lack of fusion can be seen throughout the volume.	68
Figure 41	Arrangement for repeatable length measurements of samples	81
Figure 42	Prototype of the proposed instrument for characterizing CTE	82
Figure 43	Measured width by the 2D through-beam sensor during a series of oscillations. These peaks can be easily recognized computationally, as indicated by the red dots.	83
Figure 44	Results of fitting each oscillation at room temperature and elevated temperature. A clear and consistent increase in measured width can be observed.	84
Figure 45	Finite Element Method Study of magnetic field created by N52 permanent magnet. Directional magnetic field is measured along the indicated direction.	86

LIST OF SYMBOLS AND ABBREVIATIONS

A/m	Ampere-Meter
k\$	Thousand USD
PBF-EB	Electron Beam Powder Bed Fusion
AM	Additive Manufacturing
ML	Machine Learning
CTE	Coefficient of Thermal Expansion
VSM	Vibrating Sample Magnetometer
s	Second
FORC	First-Order Reversal Curve
B	Magnetic Flux density
E	Electric Field
H	Magnetic Field
M	Magnetization
μ_0	Magnetic Constant/Vacuum Permeability
J	Intensity of Magnetization
T	Tesla
χ	Susceptibility
H_c	Coercivity
J_{sat}	Saturation Magnetization
H_{eff}	Effective Magnetic Field
H_{ext}	External Magnetic Field
N	Shape Demagnification Factor

DC	Direct Current
A	Current
H_x	Gradient of Magnetic Field (along x)
Hz	Hertz
IEC	International Electrotechnical Commission
AC	Alternating Current
AGM	Alternating-Gradient Magnetometer
Fe	Iron
Ni	Nickel
Mo	Molybdenum
DoE	Design of Experiments
GPR	Gaussian Process Regression
BO	Bayesian Optimization
H_m	Maximum (Cyclic) Magnetic Field
H_{ref}	Reference value of magnetic field for J_{sat}
N/mm	Newton-millimeter
μm	Micrometre (10^{-6} m)
MAPE	Mean Absolute Percent Error
σ_x	Standard Deviation of x
\bar{x}	Mean of x
γ	Austenite Phase
PBF-LB	Laser Powder Bed Fusion
SEM	Scanning Electron Microscope
J/mm ²	Joule-Square Millimeter

ED	Energy Density
P	Power
h	Hatch
W	Watt
LHS	Latin Hypercube Sample
EI	Expected Improvement
mA	milliampere
D_{10}	10 th Percentile Diameter of Power Size Distribution
D_{50}	50 th ...
D_{90}	90 th ...
Sa	Areal Arithmetical mean height, according to ISO 25178-2:2012
FEM	Finite-Element Method

SUMMARY

The autonomous experimentation paradigm has the potential to rapidly accelerate the development of materials and processes. It requires new characterization techniques with sufficient throughput to screen large numbers of samples. In this work, a methodology for measuring the magnetic properties of ferromagnetic samples is developed. The proposed methodology utilizes a simple, inexpensive desktop instrument designed to be amenable to automation. The use of the hardware and requisite data analysis methodology is validated and shown to have acceptable accuracy and repeatability for screening purposes; saturation magnetization is typically accurate to 1% and repeatable to 0.2%, while coercivity is repeatable to 20-30 A/m. The measurement time per specimen is under 20 seconds, with an architecture that allows significant further improvement. The cost of hardware is on the order of \$1000 US, and there are minimal constraints on the acceptable geometry of samples. These characteristics are compared to existing techniques and shown to represent a favorable tradeoff for many screening applications.

This magnetic characterization technique is then demonstrated by accelerating the development of the Electron Beam Powder Bed Fusion (PBF-EB) additive manufacturing of Permalloy, a high-performance magnetic alloy used widely in electrical machinery. Over four hundred specimens were printed and characterized, utilizing the developed technique as well as other high-throughput measurements. Additionally, Active Learning was employed, allowing many experiments to be designed efficiently and autonomously. The use of high-throughput characterization and Active Learning enabled the effects of 6 factors to be explored simultaneously, including advanced scanning strategies of the

electron beam. The effect of these factors on magnetic properties is analyzed; greater energy density and advanced scan strategies are found to result in a statistically significant increase in magnetization by approximately 1%. Four of the factors are also shown to have coupled effects on surface roughness. It is found that advanced scanning strategies can result in approximately a four-fold increase in the beam speed threshold for the onset of Plateau-Rayleigh instabilities affecting surface roughness. These results show the potential of high-throughput screening experiments to explore high-dimensional relationships and demonstrate the practical application of the developed magnetic characterization technique.

Finally, a method for the high-throughput characterization of the Coefficient of Thermal Expansion (CTE) is designed and prototyped. Initial results demonstrate the potential of the concept, which utilizes highly repeatable length measurements to eliminate the need for multiple furnace cycles when batch testing specimens. The method is shown to be a promising direction for future research that can introduce CTE characterization into an autonomous experimentation framework.

CHAPTER 1. INTRODUCTION

1.1 Motivation

The 2019 Decadal Survey of the Frontiers of Materials Research by the National Academies of Science, Engineering, and Medicine identified high-throughput screening as increasingly essential for materials research. New characterization techniques are required for optimization and exploration, where “accuracy is usually sacrificed for speed, in that traditional characterization techniques do not always maintain pace with high-throughput synthesis” [1]. In Boyce et al. (2023) it is argued that while researchers may be reluctant to use lower fidelity methods outside of current standards, cheap but informative measurements may be sufficient for Machine Learning (ML) models to recognize trends [2]. A combination of characterization techniques may also be required at different stages of research: a high-fidelity, standardized measurement can verify an optimal result arrived at with much cheaper measurements.

High-throughput methods, when combined with machine-learning, can enable autonomous experimentation, such as proposed by Boyce and Uchic (2021) for alloy development [3]. In this paradigm, specimens can be manufactured, characterized by autonomous systems, and the next iteration suggested by Artificial Intelligence. The foreseen conclusion is that a lab could autonomously translate engineering requirements into a tailored alloy, process, geometry, or even ideal combination of the three.

These capabilities are naturally complemented by Metal Additive Manufacturing (AM), as AM can rapidly synthesize new specimens with arbitrary parameters on-demand.

Thus, the Decadal Survey identifies “Developing integrated computational materials engineering capabilities together with high-throughput characterization techniques to accelerate the development to deployment cycle of AM” as one of four goals critical for the greater adoption of AM. In addition to shorter development cycles, high-throughput methodologies can also enable a more thorough exploration of AM’s vast feature spaces, which includes part geometry, composition, print parameters, and post-processing. Many current studies are limited to tens of samples, leaving significant potential for further optimization.

A major open problem is which existing measurements can or even should be integrated into an autonomous experimentation framework. Microstructural characterization in support of process-structure-property models is a critical component of materials research and will remain so. Applied to AM, such models have seen widespread success and have been necessary for the optimization of many properties [4]. However, these models do have limitations. The complex interactions of physics spanning many length scales makes it impossible to fully model the effect of the multitude of factors and co-factors governing AM processes [5]. Thus, high-throughput measurement of bulk properties of interest also hold value, such as for screening new regions, process monitoring, or validation of requirements. Ultimately a data-rich approach may prove ideal, where manufacturing diagnostics, microstructure, bulk properties, and functional performance are all integrated.

Significant progress has been made in the development of new high-throughput measurements and analyses. Microstructural measurements, while traditionally low-throughput, have benefited from advances in both computation and instrumentation [6].

For example, convolutional neural networks have been used to autonomously segment and quantify micrographs, eliminating expert labor [7]. ML has also enabled computationally cheaper surrogates of ab initio models of microstructure [8]. Measurements of mechanical properties have also benefitted from recent advances in instrumentation and analysis. Traditionally, mechanical characterization requires the machining of specimens into precise geometries and individual measurement of each specimen. Salzbrenner et al. (2017) developed an automated high-throughput pull tester for of miniaturized tensile bars [9]. Small punch testing (SPT) and microindentation have also been developed and shown to be reliable measures of mechanical properties [10]. There has also been significant interest in the high-throughput measurement of functional properties, such as electromagnetic properties, coefficient of thermal expansion (CTE), and corrosion resistance. Recently, Digital Image Correlation (DIC) has been employed to measure CTE in a highly parallelized manner [11]. Some functional properties such as resistivity can now be directly screened from libraries of thin film samples with varying composition, manufactured by combinatorial techniques such as co-sputtering deposition. This has been applied extensively to applications such as superconductor development, where thin films are highly representative of industrial application [12]. The activity of catalysts can also be measured in thin film arrays by directly measuring the concentrations of reactants pumped over the target surface with a scanning mass spectrometer [13]. A limitation to these methodologies is that thin films may poorly predict the properties of bulk specimens made by other manufacturing techniques, due to size effects and significant process dependence.

In this work we focus on magnetic properties, motivated by the importance of electrical machinery for climate and industry. Various techniques have been developed for

the high-throughput magnetic characterization of combinatorial thin-films [14]. Most applications to electrical machinery require bulk parts, however, and magnetic properties show significant dependence on geometry and processing history [15]. Thus, high-throughput characterization techniques of bulk magnetic specimens are required. Currently, materials research relies on conventional, high-fidelity approaches. For bulk specimens, the three most common instruments/techniques are ring specimen measurements, Permeameters, and Vibrating Sample Magnetometers (VSM). Ring specimens require a toroidal form and coils to be individually wrapped around each specimen, which greatly limits the throughput of this method. Permeameters relying on stray-field measurements require very precisely controlled geometries, which greatly increases the post-processing time and thus limits applicability to an automated experimentation framework. Vibrating Sample Magnetometers are comparatively more amenable to high-throughput research, with measurement times for a single hysteresis loop approximately ~30-60s. However, VSMs have practical issues limiting throughput, such as significant setup, fixturing, and calibration times which may take many minutes. This time can be partially reduced; Geng et al. used an automatic sample changer with VSM to reduce fixturing times [15]. Another limitation with VSM is that the measurement rate is fundamentally limited by the frequency of actuations, resulting in data intensive measurements such as First-Order Reversal Curves (FORCs) taking many minutes. VSM also poses a significant cost, typically in the range of 100-500k\$, which may be prohibitively expensive especially when magnetic properties are not the primary response of interest. In this work, we identify the possibility for a high-throughput magnetic characterization technique, which can possess a comparative advantage if low cost is

combined with superior throughput (such as <30s for combined measuring and setup/fixturing), along with acceptable accuracy and repeatability for at least screening applications.

To demonstrate the utility of the proposed characterization technique, it is necessary to use a sufficiently high-throughput synthesis technique. AM holds significant potential for manufacturing electrical machinery with improved cost and performance [16]. Labor intensive lamination processes could be replaced with the direct manufacturing of highly optimized geometries. Electron Beam Powder Bed Fusion (PBF-EB) is an AM technique with advantages to manufacturing electrical machinery, such as its ability to produce thin walls with minimal distortion. The process development of the high-performance magnetic alloy Permalloy is unexplored with PBF-EB and is identified as an opportunity to employ high-throughput methodologies for initial screening.

Our objective are as follows:

- To develop a high-throughput methodology for the characterization of bulk magnetic properties, with potential to be incorporated into an autonomous experimentation framework. By requiring only sufficient accuracy and repeatability for screening, superior throughput (<30s) at vastly lower cost can be achieved. Lower cost will enable magnetic properties to be routinely measured in materials research even when they may not be the primary property of interest.
- To apply this methodology to the process development of the Electron Beam Powder Bed Fusion, to demonstrate the utility of these measurements and the general

advantages of high-throughput screening studies in enabling the exploration of high-dimensional feature spaces.

1.2 Thesis Organization

This work is organized into 5 chapters and one appendix. CHAPTER 2 provides a general background on the topics covered. CHAPTER 3 and CHAPTER 4 constitute the main body of work, and each are intended as standalone studies. CHAPTER 3 details an instrument for the rapid characterization of magnetic properties. CHAPTER 4 focusses on the process development of the Electron Beam Powder Bed Fusion of Permalloy, utilizing a variety of high-throughput methodologies including that developed in CHAPTER 3. Overall conclusions and future work are discussed in CHAPTER 5. As an addition to the main body of work, Appendix A presents a technique for the high-throughput characterization of the Coefficient of Thermal Expansion (CTE) along with preliminary results.

CHAPTER 2. BACKGROUND

2.1 Electromagnetism

Classical electromagnetism is defined by Maxwell’s equations, a set of four coupled equations that relate magnetic flux density, \mathbf{B} , and the Electric Field, \mathbf{E} . These fields together can predict the force on a moving charged particle according to the Lorentz force law.

Table 1: Maxwell’s Equations of Classical Electromagnetism

LAW	DIFFERENTIAL FORM	NOTE
GAUSS’S LAW	$\nabla \cdot \mathbf{E} = \frac{\rho}{\epsilon_0}$	Electric charge density ρ , permittivity of free space ϵ_0
GAUSS’S LAW FOR MAGNETISM	$\nabla \cdot \mathbf{B} = 0$	
FARADAY’S LAW OF INDUCTION	$\nabla \times \mathbf{E} = -\frac{\partial \mathbf{B}}{\partial t}$	
AMPERE’S LAW	$\nabla \times \mathbf{B} = \mu_0 \left(\mathbf{I} + \epsilon_0 \frac{\partial \mathbf{E}}{\partial t} \right)$	Magnetic constant μ_0 , Electric current density \mathbf{I}
LORENTZ FORCE LAW (FOR REF.)	$\mathbf{F} = q\mathbf{E} + q\mathbf{v} \times \mathbf{B}$	Force \mathbf{F} , charge q , velocity \mathbf{v}

Electrons bound to atoms can act as a current loop, which can be approximated from the microscale upwards as a continuum of magnetic dipoles. The degree of alignment of these dipoles can result in net magnetization. This alignment and thus the magnetization is affected by \mathbf{B} . Conversely, this magnetization will affect the \mathbf{B} field. To separate these effects, constitutive equations for magnetism of real materials thus need to introduce a new quantity, \mathbf{H} , the magnetic field (also called the “magnetizing field”), which is defined in terms of \mathbf{B} less the Magnetization \mathbf{M} (Equation 1). Note μ_0 is the magnetic constant, or

“vacuum permeability.” In this work we use the SI definition of μ_0 , where $\mu_0 = 4\pi \times 10^{-7} \text{N/A}^2 \approx 1.26 \times 10^{-6} \text{N/A}^2$.

$$\mathbf{H} = \frac{1}{\mu_0} \mathbf{B} - \mathbf{M} = \frac{1}{\mu_0} (\mathbf{B} - \mathbf{J}) \quad (1)$$

Here we further introduce the Intensity of Magnetization \mathbf{J} , which is equal to $\mu_0 \mathbf{M}$. The SI units for \mathbf{H} and \mathbf{M} are Ampere-Meters [A/m], and Tesla [T] for \mathbf{B} and \mathbf{J} . For a paramagnetic material, \mathbf{M} is proportional to \mathbf{H} by the magnetic susceptibility χ such that:

$$\mathbf{M} = \chi \mathbf{H} \quad (2)$$

While analytically appealing due to the linear relationship and reversibility, paramagnetism is generally a very weak effect. Instead, electrical machines rely on ferromagnetic materials for performance, which can achieve much greater magnetizations.

2.2 Ferromagnetism

Ferromagnetic materials are defined by the spontaneous alignment of magnetic dipoles into magnetic domains below the curie temperature T_c . Iron, Nickel, and Cobalt are all ferromagnetic at room temperature. These are sequential on the periodic table, their properties due to the band structure of these transition metals; see [17] for a review of the atomistic origins of ferromagnetism. These three elements are ubiquitous in most ferromagnetic alloys as well. Magnetic fields will cause shifts and rotations in the magnetic domain structure, resulting in net magnetization. This magnetization is a partially

irreversible process, and ferromagnetic materials exhibit hysteric behavior under cyclic fields.

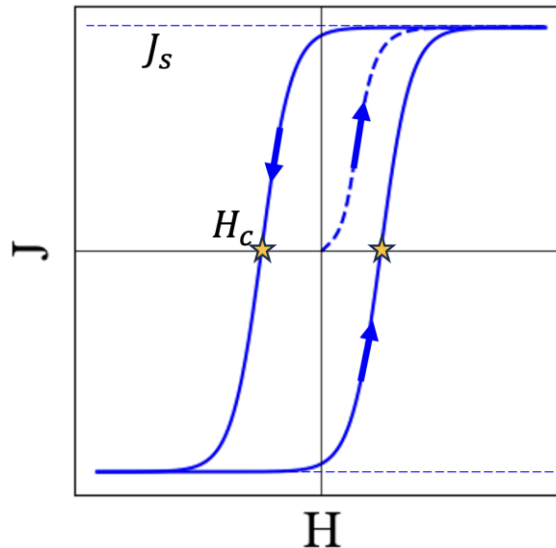


Figure 1: Representative hysteresis loop of a ferromagnetic material.

Figure 1 illustrates the typical qualities of an archetypical magnetic hysteresis loop. The initial magnetization is approximately linear and reversible, with a slope equal to a constant susceptibility χ . This initial magnetization is generally identified with the bending of magnetic domain walls, analogous to elastic deformation in mechanics. The slope increases greatly after the reversible regime, until it begins to asymptotically approach the saturation magnetization J_{sat} . This magnetization is associated with irreversible rotations and translations of magnetic domain walls. The saturation magnetization acts as an upper limit on magnetization, corresponding to maximal alignment of magnetic domains. From a saturated state, a backfield with magnitude defined as the coercivity H_c will be required to fully demagnetize the sample to $J = 0$. A complete magnetic hysteresis loop consists of two half loops, which typically have the same values of J_{sat} and H_c . Thus, H_c defines the halfwidth of the hysteresis loop. Greater J_{sat} is favorable for electrical machinery, while

the ideal H_c depends on the application. Low H_c will reduce power losses under cyclic fields, while greater H_c is favored when demagnetization is undesirable. These define “soft” and “hard” magnets respectively.

2.3 Shape Demagnetization Effect

The magnetic field produced by a magnetized sample is called the “stray field” outside of its volume, and the “demagnetizing field” inside. It is so-called demagnetizing because it will act to reduce the external magnetic field. This effect can be captured by a shape demagnetization factor N , a dimensionless constant. The effective field H_{eff} can be defined as the external field H_{ext} less than demagnetizing field:

$$H_{eff} = H_{ext} - N \frac{J}{\mu_0} \quad (3)$$

This results in the shearing of the magnetic hysteresis loop, as shown in Figure 2. The shape demagnification effect is important to account for as it will significantly reduce magnetization in many instances. Generally, N will be lesser for samples with a greater aspect ratio in the direction of magnetization, and greater otherwise.

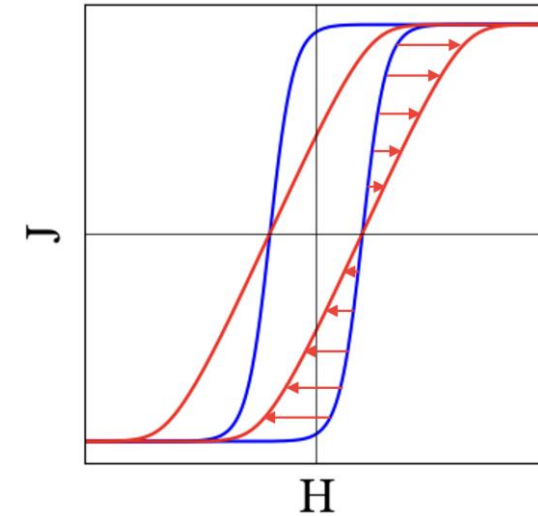


Figure 2: Shearing of hysteresis loop due to the shape demagnification effect. Blue - J vs. H_{eff} ; red - J vs. H_{ext}

2.1 Frequency Effects

The magnetic hysteresis loop can be measured in a quasistatic or “DC” manner without any dynamic effects. However, in many applications of electrical machinery cyclic fields can occur at high frequencies for which dynamic effects become significant. One such effect is Eddy currents; per Lenz’s law, these will act to reduce the effective field.

2.2 Magnetic Characterization of Bulk Ferromagnetic Samples

The magnetic characterization of bulk samples typically relies on one of three operating principles, shown in Figure 3. One is the magnetic circuit: the specimen forms a closed circuit, with two separate coils wound around a section. A driving current through one coil creates a constant magnetic flux throughout the entire circuit. A pickup coil can then measure the change in flux from the induced voltage according to Faraday’s law. A consequence of using a closed magnetic circuit is that there is no shape demagnification effect. A magnetic circuit is commonly achieved with a solid ring specimen, as shown in

Figure 3. A second approach is stray field measurement. The sample is placed in a near-uniform field (such as at the center of a larger electromagnetic coil), and the stray field is measured with a Hall Probe or other magnetometer.

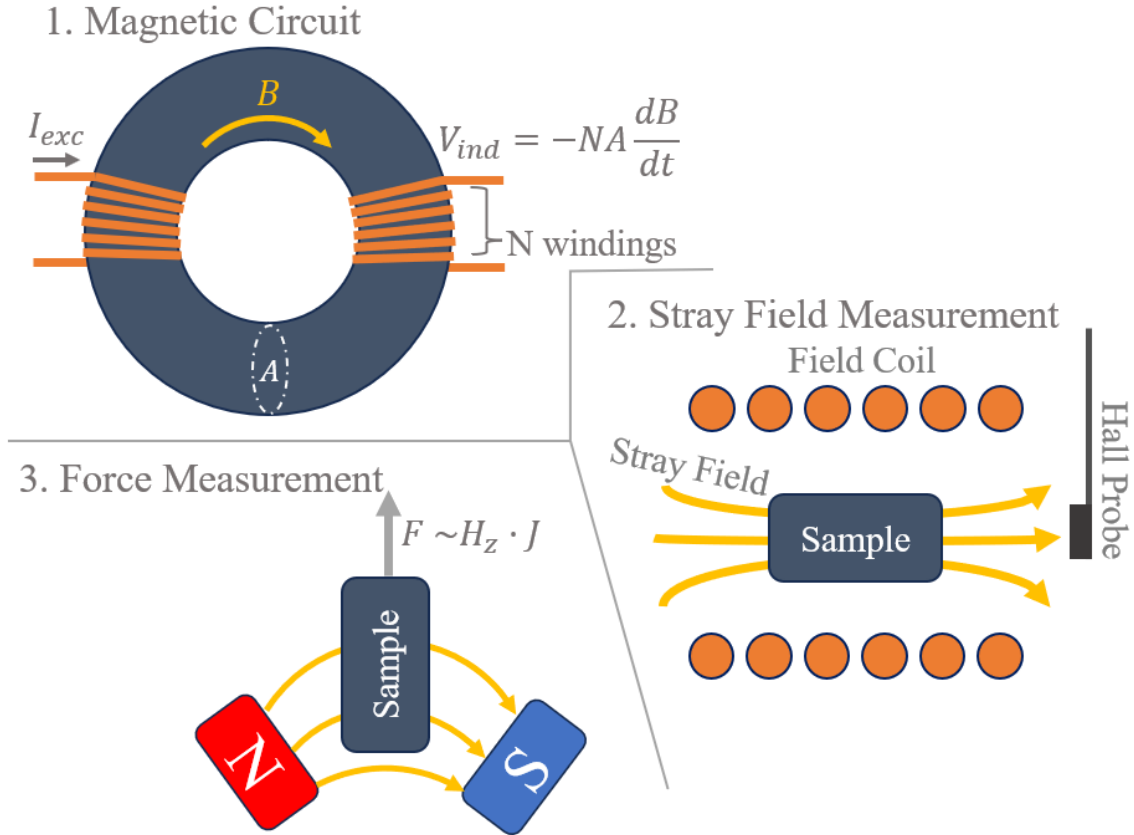


Figure 3: Simplified representations of the most common operating principles for the characterization of bulk ferromagnetic samples.

Another approach is to measure the force on a sample due to a graded magnetic field, in order to calculate the magnetization. Figure 3 depicts a simplified version of the Faraday balance, one of the earliest such devices. The force on a sample in a graded field is as follows:

$$F = JV \frac{\partial H}{\partial x} \quad (4)$$

where V is volume. Thus, the force is proportional to its magnetization and the gradient in magnetic field. If the force, gradient, and field are known, then J can be related to H .

2.2.1 Vibrating Sample Magnetometer (VSM)

VSM operates by actuating a specimen within a uniform field (Figure 4). Pickup coils then measure the stray field generated by the sample inductively according to Faraday's law. VSM is extremely versatile and accurate, and used for a wide range of applications including materials research [18]. The measurement time of a single datapoint is fundamentally limited by the frequency the sample can be actuated (typically 10-100Hz). It is common to be able to rotate the specimen along the axis of actuation; this allows for two-dimensional magnetization histories to be considered.

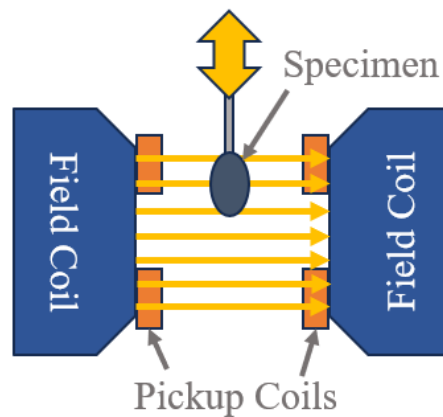


Figure 4: Simplified schematic of a Vibrating Sample Magnetometer

2.2.2 *Coercimeter*

Coercimeters as defined by IEC 60404-7 operate on the principle of stray field measurement, however they solely measure the coercivity. This is accomplished by saturating the sample, and then applying an increasing reverse field until the stray field is null. As only coercivity is measured, which is invariant in the shape demagnification shearing transformation (Figure 2), this is a geometry independent method [19].

2.2.3 *Alternating Gradient Magnetometers (AGM)*

AGMs utilize the principle of force measurement shown in Figure 3. AGM's feature a pair of large DC electromagnets to create a uniform field, and pair of opposing AC coils in between which create a slight, alternating gradient. The sample is mounted on a glass cantilever in the center; by alternating the field at the resonance of the cantilever, highly sensitive measurements can be achieved [20]. AGM's are typically used for feebly magnetic or low volume samples such as thin films

2.3 Electron Beam Powder Bed Fusion

Electron Beam Powder Bed Fusion (PBF-EB) is an Additive Manufacturing (also known as "3D Printing") process where an electron beam is focussed and deflected by electromagnetic lenses to selectively fuse powder. Powder is spread level over the build area and fused in successive layers. Charges accumulating on the powder create repulsive Coloumb forces which can lead to "smoke-out" events where the powder spontaneously disperses [21]. To resist this, the powder in the print area must be regularly heated to sinter

the powder. Thus, PBF-EB is a hot process, and additionally requires high vacuum to prevent interference with the beam.

In Figure 5 the major elements of PBF-EB are shown. Exact mechanical implementation can vary; for example, in some commercial systems, powder is dispensed from a hopper from above the build plane rather than raised by a powder piston from below.

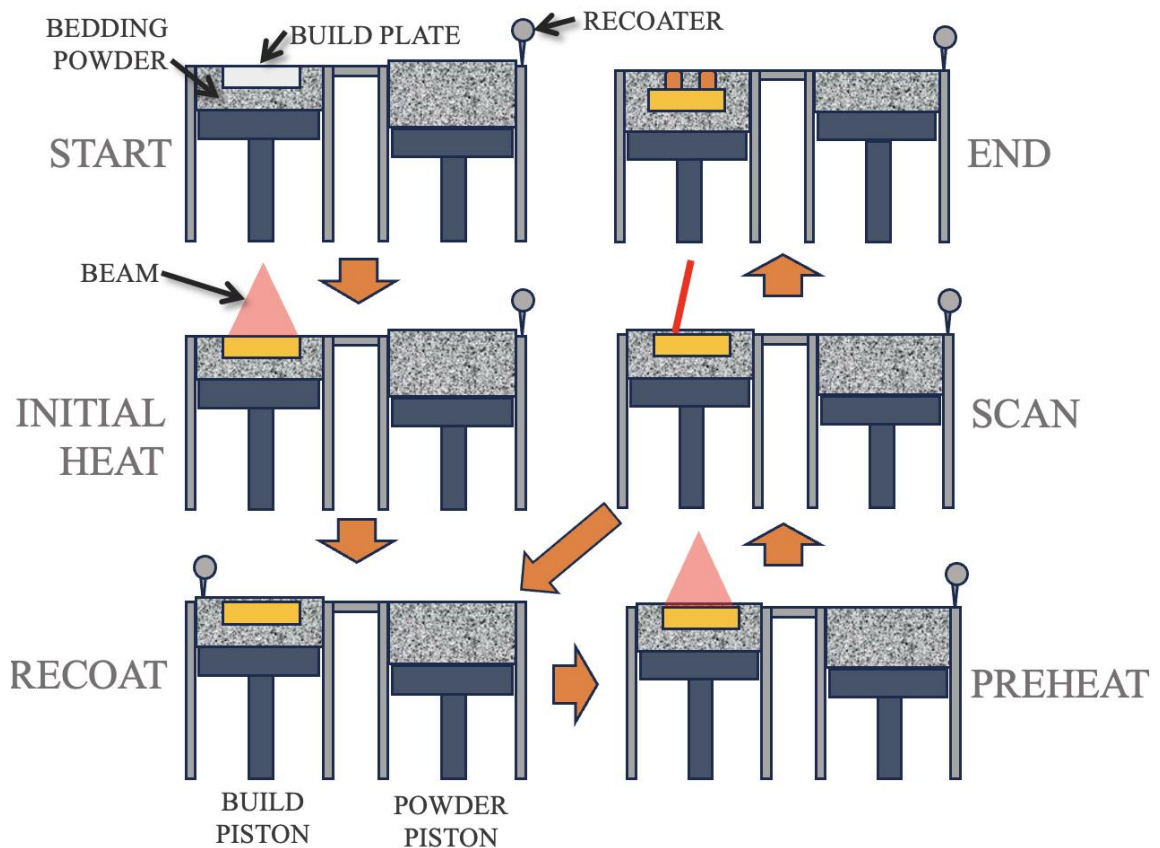


Figure 5: Schematic of the PBF-EB Process. To avoid a “smoke-out” event, the plate is first heated by diffuse beam to a temperature which will lightly sinter the powder. The recoater sweeps powder from the powder piston to the build piston, which is then preheated by diffuse beam. A concentrated beam then scans the desired patterns, and the pistons actuate to enable another coating of powder.

2.4 Permalloy

Permalloy is a Nickel-Iron ferromagnetic alloy, with excellent soft magnetic properties that have made it ubiquitous in electrical machinery. While “Permalloy” can refer to a few different exact compositions such as Fe₈₀Ni₂₀, greatest magnetic performance is achieved with FeNi₂₀Mo₄, also called “Supermalloy.” For wrought Permalloy, predominantly γ -Ni is expected. Coarser grain structure is generally desired as it results in easier domain wall movement and thus lower coercivity [22].

2.5 Active Learning Approaches for Materials Research

Currently, materials research often requires an “expert-in-the-loop.” An expert will analyze the results of a set of experiments, and utilizing best judgement will select a design for the next experiment. Experimental designs can be chosen according to classical Design of Experiments (DoE), such as defined in The National Institute of Standards and Technology (NIST) Handbook of Statistical Methods [23]. These known experimental designs allow for rigorous, pre-planned studies for a variety of objectives, such as screening or optimization. Typically, these designs use a linear function or low order polynomial to model the response surface from a small number of factors. Materials research, however, often requires more complex models with many factors that govern materials and processes. Recent computational advances have enabled Machine Learning (ML), which can model non-linear response surfaces in high dimensions. ML has found widespread use in materials research, for modelling as well other applications such as process monitoring [24]. New DoE techniques have been developed to efficiently train these models. This includes Active Learning, where an acquisition function allows new points for sampling to

be optimally selected. Active Learning has clear application to autonomous experimentation, where it can reduce the need for an expert-in-the-loop. Two of the most common ML approaches applied to materials research are Neural Nets (NN) and Gaussian Process Regression (GPR) [25, 26]. Neural networks can fit arbitrarily complex response surfaces, but may be vulnerable to overfitting the small and high variance datasets often found in materials research [27]. Gaussian Process Regression, by contrast is robust, flexible, and applicable to smaller datasets. It has an inherent characterization of uncertainty, which allows it to be easily extended into Active Learning with Bayesian Optimization (BO). BO is well suited for physical experiments, and GPR/BO have found success in materials development, such as in Herbol (2020), where it was shown BO more optimally selected new points for evaluation than conventional methods [28].

CHAPTER 3. NOVEL TECHNIQUE FOR THE HIGH-THROUGHPUT CHARACTERIZATION OF SOFT MAGNETS

3.1 Introduction

Soft magnets are those which can be easily magnetized and demagnetized or have their polarity reversed. Soft magnets are ubiquitous in electrical machines, such as the stator of an AC motor, or the laminations of a transformer. The magnetic properties of these materials are critical for the performance and energy efficiency of these devices. One such property is the coercivity, a measure of magnetic softness that also corresponds with energy losses under cyclic fields. Electric motors alone consume over 40% of the world's electrical energy [29]. Consequently, there is a strong motivation to optimize these properties and their tradeoffs, such as with mechanical properties and manufacturability. We are interested in the high-throughput characterization of these properties, to accelerate the discovery of novel materials and manufacturing processes.

A multitude of instruments have been developed to characterize the magnetic properties of samples, such as the Vibrating Sample Magnetometer (VSM). While many of these existing techniques are extremely high fidelity, a gap exists for a system with all the following qualities:

- High-throughput
- Minimal geometry and surface condition constraints on test samples
- Measures both magnetic saturation and coercivity
- Low cost, desktop system

Table 2 compares relevant techniques by these criteria. It should be noted that many of these values are approximations or estimates, and the criteria specifically pertain to the application of screening bulk ferromagnetic samples. Some specific considerations are neglected. For example, ring specimens have the advantage of not being affected by the shape demagnification effect, a geometric factor which reduces the effective magnetic field on a specimen (see 2.3). “Dimensions” refers to the ability to control the magnetic field in multiple dimensions for more complex histories. “Sample Size” is concerned with the minimum size of specimens required beyond a representative bulk specimen, which we consider to be on the order of mms. Evaluating throughput, some techniques are noted to require significant setup time. This generally refers to some combination of calibration, machine initialization, and fixturing times. Measures of fidelity are also not included in this comparison. All compared measurements are superior in this regard to the proposed instrument.

Table 2: Comparison of magnetic characterization techniques on basis of high-throughput screening of bulk samples.

CAPABILITY/ REQUIREMENT	RING	VSM	COERCIMETER	AGM	PROPOSED
FREQUENCY	DC to MHz	DC to Hz	DC	DC to Hz	DC
DIMENSIONS	1D	2D	1D	1D	1D, 3D potential
SAMPLE SIZE	~10-100mm	<10mm	<10s of mm	<5mm	1-5mm,
FORM + CONDITION	Toroidal topology	Needs to be robust to high accelerations	Minimal	Uniform and defined, narrow profile	Minimal
THROUGHPUT	Very low-windings required	30-60s + minutes setup	30-60s	30s-minutes + minutes setup	<30s
SYSTEM SIZE	Desktop	Bench	Bench	Bench	Desktop
COST	Low	>100k\$	~50-100k\$	>100k\$	~1-20k\$

A technique with the qualities proposed in Table 2 would benefit exploratory research into novel materials and manufacturing processes. Increasing throughput allows larger feature spaces to be explored in more expansive studies. It is additionally necessary to reduce requirements on specimen form and finish, to avoid other bottlenecks in materials research. For example, specimens manufactured by Additive Manufacturing (AM) often have very rough surfaces that might otherwise require significant post-processing for certain characterization techniques. Minimizing the specimen size can also decrease manufacturing time and usage of limited material. A consequence of the high cost of existing instrumentation is that studies not primarily interested in magnetic properties will rarely characterize them. Many other properties, such as the coefficient of thermal expansion (see Appendix A), can be closely coupled with magnetic properties [30]; wider use of magnetic characterization could yield diverse benefits.

In this work, we develop the theory and design behind an instrument which rapidly measures the magnetic hysteresis loops of imprecise, miniaturized specimens; while this comes at a cost in fidelity, the accuracy and repeatability are quantified for various materials and shown to be sufficient for widespread screening and exploration applications.

3.2 Materials and Methods

A variety of wrought and additively manufactured specimens are characterized by the developed instrument. From the resultant magnetic hysteresis loops, the intensity of magnetization J_{sat} and coercivity H_c are measured, to assess the accuracy and repeatability of these measurements.

To assess the accuracy and repeatability of the measurement of intensity of magnetization J_{sat} , 15 specimens with known J_{sat} are characterized by the proposed instrument. These specimens had previously been cut from a component manufactured by Laser Powder Bed Fusion (PBF-LB) with a graded composition from Hiperco[®]50 [31] to Hymu80 [32], and exhibit a wide variety of properties. 7 of the 15 specimens had further been annealed. The specimens were approximately 3x3x1mm cuboids, with volumes ranging from 7.1 mm³ to 11.6 mm³. Initial characterization was done using a 14T DynaCool PPMS with VSM Option. These measurements were done at room temperature with a 5 Quadrant sweep to ± 5 T with a sweep rate of 10 mT/s.

A Fe6Si (Wt %) Silicon Steel AM ring specimen is used to assess the accuracy and repeatability of the coercivity measurements. The ring was pre-charactered at 10 Hz and $H_m = 500$ A/m. The low but non-zero frequency and incomplete saturation achieved at a low H_m both will slightly affect H_c , but in an opposite manner with a net effect assumed to be negligible. A 4.39x3.85x1.80mm cuboid is cut from the ring for testing on the proposed instrument. Two additional specimens with varying aspect ratios (4.07x3.84x1.86mm, 3.9x3.89x1.84mm) are then also tested to assess possible shape biases, comparing J_{sat} and H_c .

As a reference to assess the accuracy and repeatability of coercivity measurements near $H_c = 0$, a 4.5x3.5x1mm wrought Fe80Ni4Mo Permalloy specimen from Espi Metals was annealed per specifications of the supplier [33] and tested 10 times. One of the 15 graded samples with a coercivity of approximately 900 A/m is also tested 10 times, to measure the repeatability of H_c at greater values as well.

To realistically assess the repeatability when applied to as-printed, unfinished AM samples, 6 Fe80Ni4Mo Permalloy specimens are printed via Electron Beam Powder Bed Fusion on the same build plate with identical parameters. These specimens are nominally 3x3x3mm and snapped directly off the build plate with the only post-processing being sandblasting. They have a low density of ~80%, and poor surface condition. J_{sat} and H_c are measured for each.

3.3 Theory and Design

3.3.1 Architecture Selection

To allow for specimens with imprecise, unprocessed forms, we choose to rely on the principle of force measurement in a graded magnetic field. This decision is motivated by major limitations with alternative architectures. For example, another possibility is directly measuring the magnetic field external to a magnetized specimen, known as the “stray field.” This will be highly dependent on the geometry, however, and instruments utilizing stray field measurements will require tightly prescribed geometries. Another common architecture is to use a specimen with toroidal topology such that it acts a “magnetic circuit,” with constant magnetic flux. This inherently imposes a major limitation on possible geometries, which may not be ideal for manufacturing or measuring other responses.

Rather than using electromagnets to create an alternating gradient as in an Alternating Gradient Magnetometer (AGM), however, two opposing permanent magnets are manipulated to control the field and gradient along an axis. This configuration comes with a few disadvantages: using permanent magnets limits application to quasi-static or

very low frequency measurements, and electromagnets can generate greater fields than permanent magnets. However, as we are focussed on characterizing bulk soft magnetic samples, such sensitivity is unnecessary, and soft magnets with favourable shape demagnification factors can still be saturated or near saturated by a permanent magnet. The benefits of such an architecture are numerous: unlike Vibrating Sample Magnetometers (VSM) or AGM, measurement can be completely continuous, limited only by the sampling rate of force and position and any noise from dynamic effects. Size, complexity, and cost are significantly reduced. In AGM, by contrast, the alternating poles necessarily separate the sample from the DC poles, which necessitates them to be very large while limiting sample dimension to be being thin along the graded axis. Another consequence of this architecture is the potential for controlling the field in multiple directions, either by having multiple sets of permanent magnets or rotating the pair of permanent of permanent magnets together. The combination of continuous measurement and multi-dimensional magnetization would enable the high-throughput characterization of complex magnetization histories and other data intensive measurements.

3.3.2 *Theory*

We consider the arrangement shown in Figure 6, with a sample located between two opposing permanent magnets. Given the position of the sample relative to both magnets, the field and gradient can be calculated analytically or computationally. In this work, field and gradient are calculated computationally, the details of which are given as in 3.3.3 and Appendix B. J can be calculated from the force on the sample utilizing Equation 4. This requires the volume of the sample, which can be calculated from density testing.

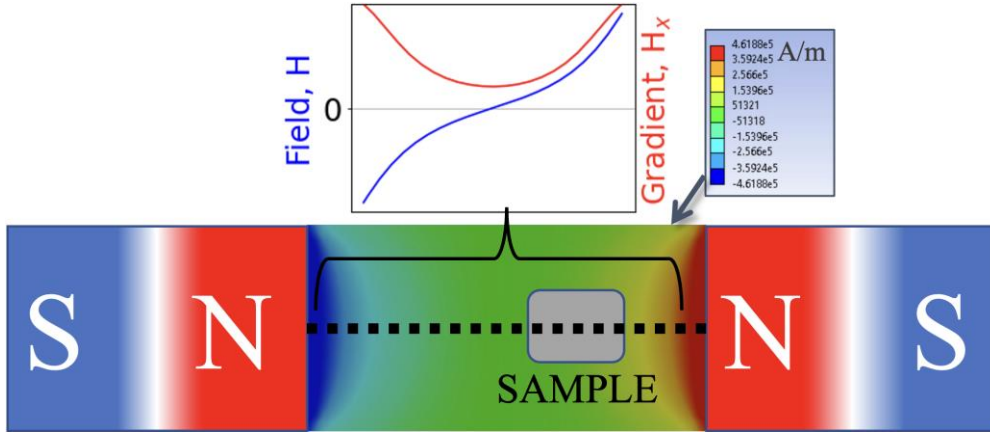


Figure 6: The magnetic field H in the x-direction (dashed) and magnetic field gradient H_x between two opposing permanent magnets. Near the central axis these quantities will be relatively uniform over an area perpendicular to this axis.

By manipulating the position of these permanent magnets along an axis, the magnetic field applied to the sample can be made to vary cyclically with time up to a limit of H_m as shown in Figure 7. This field will be affected by the demagnetizing field of sample (see 2.3). We identify the field purely created by the permanent magnets as H_{ext} , the external field, and conversely H_{eff} is the effective field accounting for shape demagnification effects.

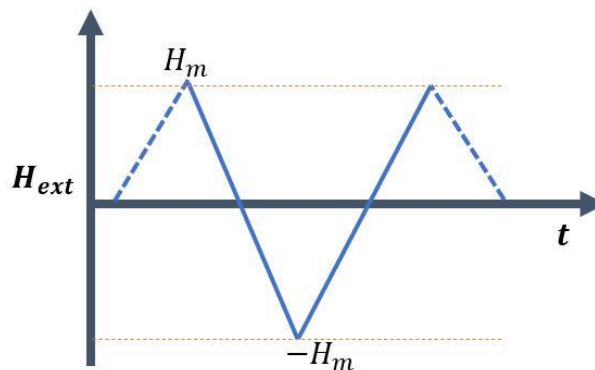


Figure 7: Representative evolution of $H_{ext}(t)$. The solid lines represent a complete hysteresis loop. H_m is the maximum cyclic field applied.

3.3.2.1 Calculation of coercivity H_c

For a typical hysteresis loop, when $J \approx 0$ there is an approximately linear relation between J and H . In Figure 2 this can be seen as the near constant slope near the intercept with the $J = 0$ axis. Additionally, we expect the two half loops to possess equal and opposite coercivity. Thus, when $J \approx 0$:

$$J^\mp(H_{eff}) = \mu_0\chi(H_{eff} \pm H_c) \quad (5)$$

where χ is a constant magnetic susceptibility. Equation 5 is in terms of the effective field, H_{eff} . By substituting H_{ext} (see Equation 3), we can arrive at the following:

$$J^\mp(H_{ext}) = \frac{\mu_0\chi}{1 + \chi N} (H_{ext} \pm H_c) = A(H_{ext} \pm H_c) \quad (6)$$

where N is the shape demagnification factor. We simplify the various constants into a single factor, A . Equation 6 does not directly apply, however. A difficulty of modelling the system shown in Figure 6 is that there is a large gradient in the external field over the length of sample. Furthermore, we assume the exact geometry of the sample is not precisely known.

To analyze this problem, we consider an arbitrary coordinate system in the reference frame of the sample, such that the x -axis is aligned with the primary direction of the magnetic field. If we assume the external field has a constant gradient H_x over the length of the sample, we can divide the external field into a constant and graded component, based on some reference value of x we label ξ (Figure 8):

$$H_{ext}(x) = H_{ext}(\xi) + H_x \cdot (x - \xi) \quad (7)$$

$H_{ext}(\xi)$ is the “constant component,” whereas $H_x \cdot (x - \xi)$ is now referred to as the “graded component.”

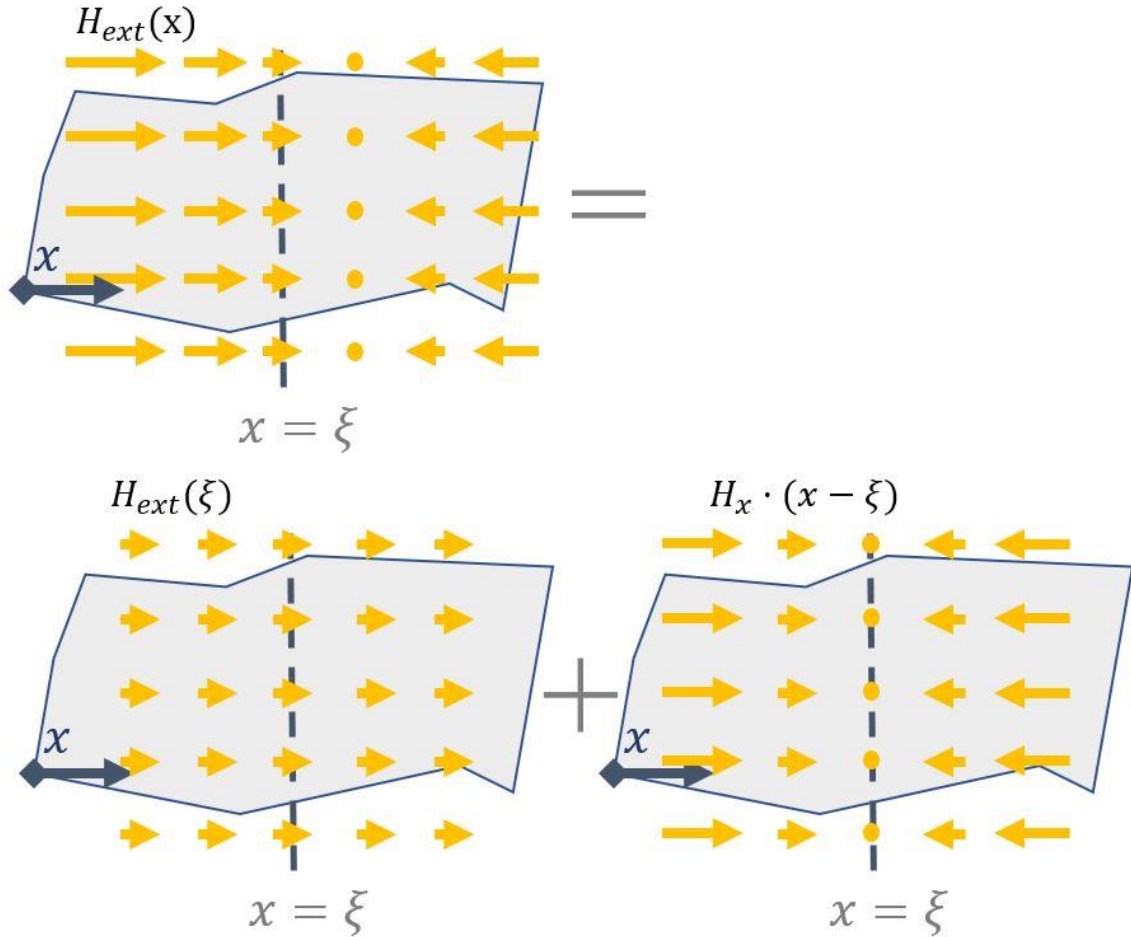


Figure 8: Decomposition of the external field H_{ext} into a constant and graded component based on sample coordinated. It is assumed that the gradient in H_{ext} is constant over the length of the sample, equal to H_x

Because of the approximately linear relationship between J and H in this region, we can decompose J into a superposition of the effects of the graded and constant components. It should be noted J is not constant across the sample, except for certain

geometries. Instead, we consider the volume averaged mean value, \bar{J} . Once source of error is that even if this mean $\bar{J} \approx 0$, there may be portions where local J is much greater and non-linearities emerge.

From this decomposition, we now have the effect of a constant field $H_{ext}(\xi)$, for which Equation 6 applies, and the unknown effect of a graded component. From the intermediate value theorem there should be a value of ξ such that the volume averaged magnetization \bar{J} (in x) contributed by this graded component is 0 and thus contributes no net force on the sample (Equation 4). It is important to note that local J from the graded component will vary throughout the sample; only overall will it cancel out. It can be roughly considered that each end of the sample will be magnetized opposite, though in reality the local J may vary in a more complex manner. Through careful selection of ξ , we can thus eliminate the effect of the gradient and simply use Equation 6 to fit for the coercivity; this applies even for an arbitrary geometry in a graded field.

We further expect $x = \xi$ to take on the same value for both half loops from symmetry: referring to Figure 7, we expect the exact same evolution from $H = H_m$ to $H = 0$ as $H = -H_m$ to $H = 0$. This is because we assume quasi-static behavior, so each evolution is identical except for an arbitrary minus sign. A source of error will be if there is any slip in the sample relative to how we define the sample coordinates (which will in practice be done relative to the sample mounting interface). To constrain the problem sufficiently such that ξ can be solved for, we assume that H_c is exactly equal for both half-loops, which will uniquely determine a value of ξ (Figure 9).

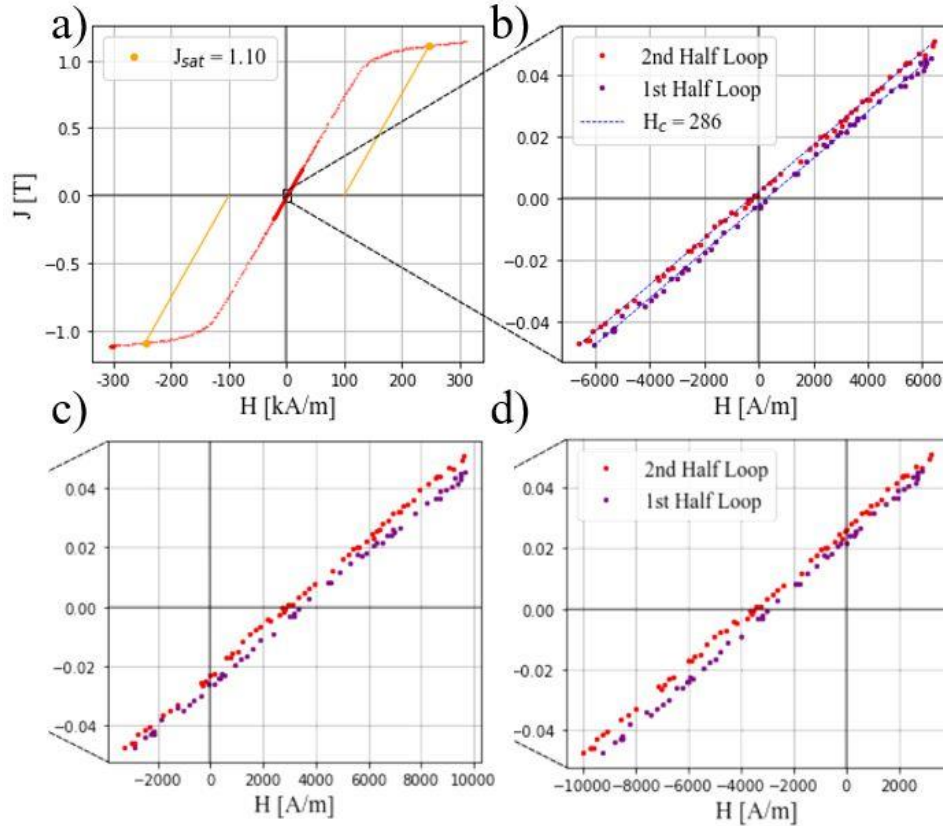


Figure 9: Demonstration of the effect of ξ , showing how it is constrained by the equal and opposite coercivity condition. a) Complete magnetic hysteresis loop. b) Inset of (a) with correctly calculated ξ . c) .. with underestimated ξ . d) .. with overestimated ξ .

Coercivity is thus found in the following manner:

1. Find the locust of points from both half loops such that $|\bar{J}| < \delta$ for small δ (typically 0.03T)
2. Fit for H_c , ξ , A , minimizing the sum square error

This yields the coercivity H_c , but also ξ and A which will be necessary for the next set of calculations for J_{sat} .

3.3.2.2 Calculation of J_{sat} and hysteresis loop

We continue to use $x = \xi$ as the reference position for the definition of H_{ext} . Recall that was based on assumption of $J \approx 0$, however it should still serve as a reasonable

definition elsewhere. The exact definition of H will matter less as the entire volume becomes fully saturated.

If the sample geometry is not known and therefore N can't be calculated, it must instead be approximated. We do this by assuming that $\chi \gg N$, where χ is the susceptibility of each half loop at $\bar{J} \approx 0$. This is a very reasonable assumption, though will create a small shearing error in the final hysteresis loop (from the approximation below). We can now simplify the constant A as follows:

$$A = \frac{\mu_0 \chi}{1 + \chi N} \approx \frac{\mu_0}{N} \quad (8)$$

From Equation 3, we can now correct for the shape demagnification effect as follows:

$$H_{eff} = H_{ext} - \frac{\bar{J}}{A} \quad (9)$$

$$\leftrightarrow \bar{J} = A(H_{ext} - H_{eff}) \quad (10)$$

Equation 9 can be used to correct for the shape demagnification shearing transformation. In practice we will use Equation 10 to plot lines with constant H_{eff} , which will illustrate the estimated value of N as well.

Because N will vary somewhat between irregular specimens, max cyclic field H_m will also vary across specimens. For comparability we can approximate J_{sat} as $J(H_{eff} = H_{ref})$, where $H_{ref} < H_m$ is a large value that is still achieved across a set of specimens, such as 100 kA/m . If full saturation is not realized at H_{ref} , J_{sat} will be an underestimate.

3.3.3 Implementation

The instrument is sized ideally for specimen with a volume of $\sim 10 - 50 \text{mm}^3$, existing within a $4 \times 4 \times 4 \text{mm}$ envelope. This size is based on the smallest geometries successfully studied in prior art [15].

A device is realized as shown in Figure 10. Two opposing Neodymium Grade N52 permanent magnets with a remnant magnetic flux density B_r of 1.44T are used to create the graded magnetic field. These have dimensions of $\phi 25.4 \times 25.4 \text{ mm}$. Ansys Finite-Element Method (FEM) simulations are used to numerically determine the field created by each magnet along the axis of interest. From this result and the positions of the magnets, the magnetic field can be calculated. Details of these calculations and FEM simulations are reviewed in Appendix B. These simulations are further used to optimally design and size the instrument, by best realizing the assumptions 3.3.2 such as constant gradients and magnetic fields entirely dependent on x over the dimensions of a specimen. For example, it was found there was generally a 2% variation in field across a $4 \times 4 \text{mm}$ cross section centred perpendicular to the main axis, except where this field is near zero.

These permanent magnets are mounted to two linear actuators driven by stepper motors, which provide positional control; the actual position, however, is measured by the through-beam sensor for greater precision.

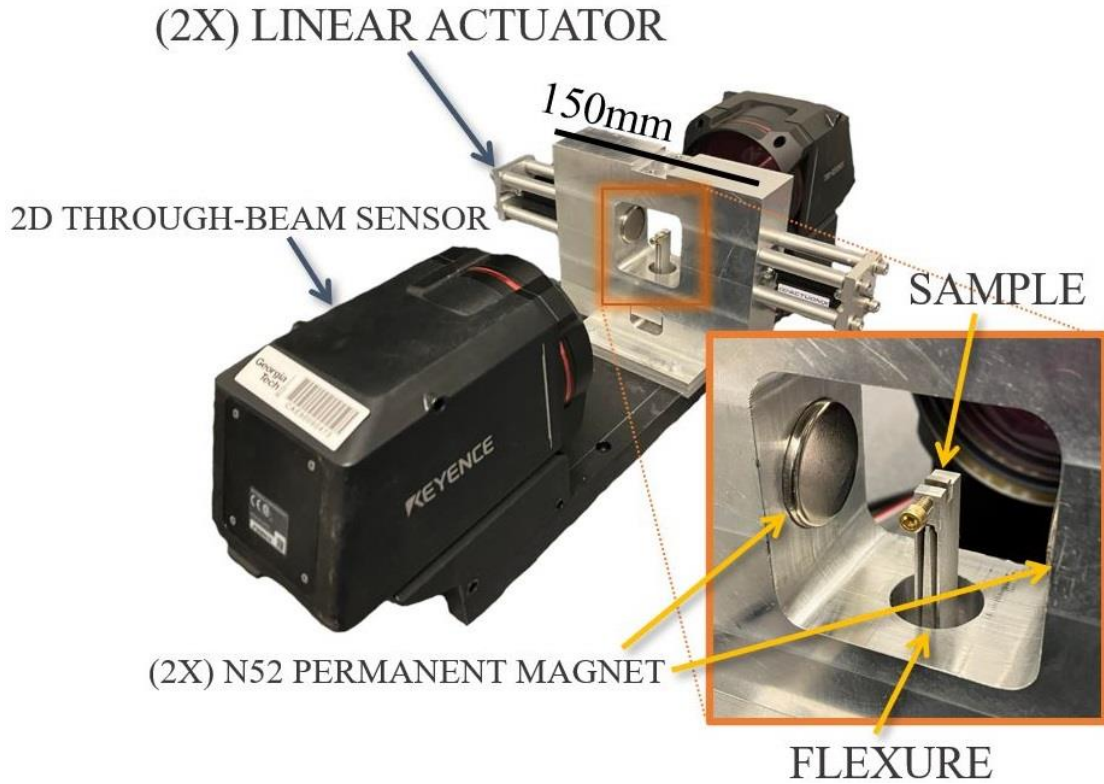


Figure 10: Physical realization of proposed instrument

Figure 11 shows a detailed view of instrument. A flexure is used to measure the force on the sample, as calculated from its deflection (in assumed direction of field) and stiffness. This flexure is the sole element reacting the force on the specimens, and a parallel beam architecture is used. The stiffness is estimated analytically, but then calibrated using reference specimens with known J_{sat} ; this may also act to account for other errors in system (such any deviation in the remanence of the permanent magnets from expected) and thus ensure proper scaling.

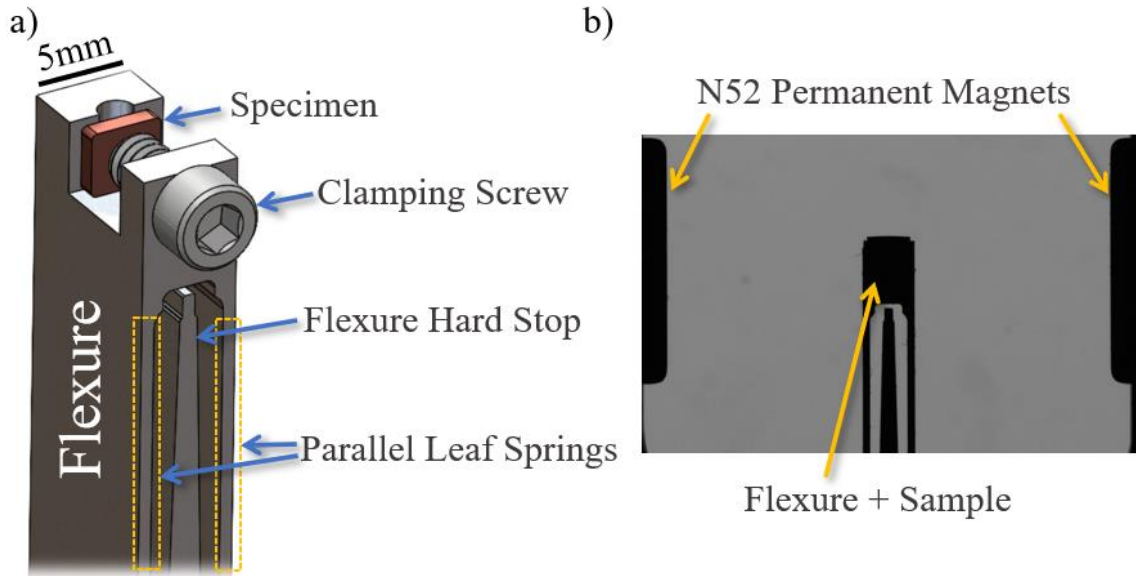


Figure 11: a) Detail view of flexure and specimen mounting b) View of flexure, magnets from through-beam sensor. The deflection of the flexure is calculated, as well as the position of each magnet relative to the median of the flexure.

Samples are mounted to these flexures, using a brass or Nylon mounting screw. 3 aluminium flexures with approximate stiffness values of 5 N/mm, 2.7 N/mm, and 1.3 N/mm are manufactured as are appropriate for different specimen sizes. Vibrations of the flexure may add significant noise to the results. To account for this, a low-pass filter below the first mode of the flexure is used to filter the measured deflections, though in practice this is only necessary for the 1.3 N/mm flexure. An access port from above and customized tooling with a magnetic mount are used to quickly load samples into place.

The relevant cross section including the flexure and two magnets is monitored by a 2D Through-beam sensor, the Keyence TM-X5065. The positions of the two magnets relative to the top portion of the flexure are measured, as well as the deflection of the flexure. The exposure time is 100us and sampling rate is approximately 70 Hz; the latter is mostly determined by the time required to process the images and extract measurements.

The through-beam sensor was chosen for these measurements to ensure positional measurements and the calculated flexure deflection are perfectly synchronous, and additionally to give flexibility during development. Alternative measurements such as strain gauges could have been used and likely would be more appropriate for a subsequent model.

Figure 12 and Figure 13 shows the actual and measured positions over the course of the course of a typical hysteresis loop measurement. Actuation is slowed for the portions used to compute coercivity. It can be seen that the total measurement time is less than <20 seconds. Given a reasonable amount of time to load, retrieve, and organize samples, a throughput of 1 specimen/<30 seconds is highly practical.

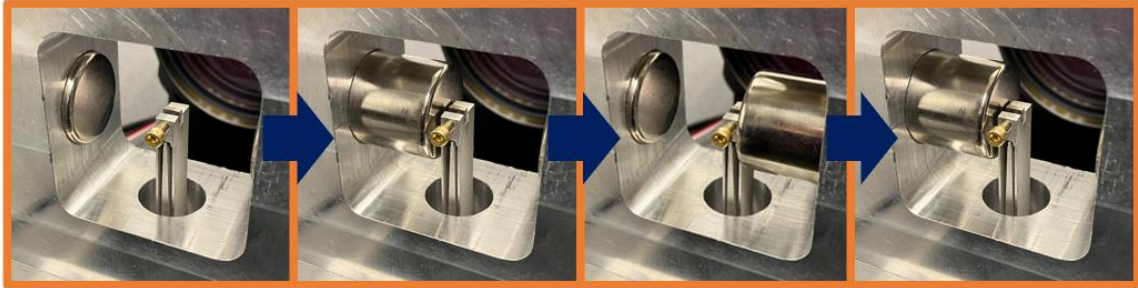


Figure 12: Actuation sequence of the permanent magnets, for a complete cycle

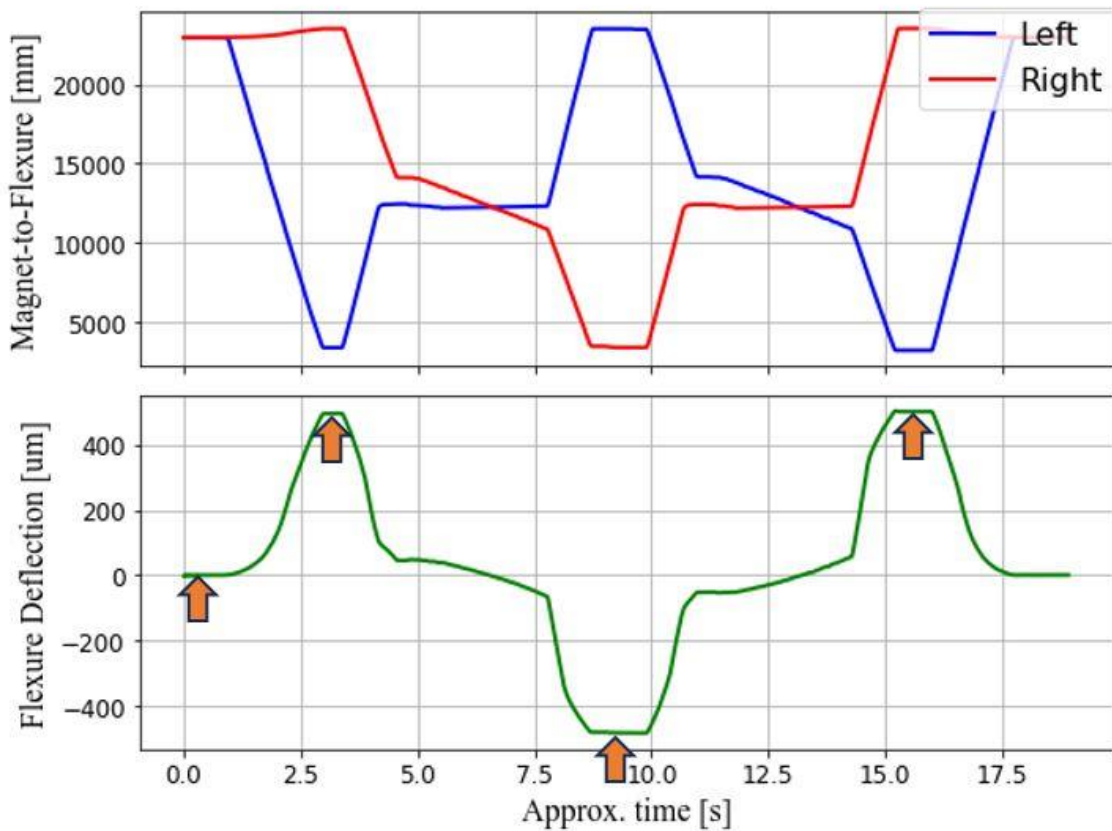


Figure 13: Actuation of the magnets vs. flexure deformation, typical response. Arrows indicate the locations of the sequence of images shown in Figure 12. Between the two positive peaks is one complete hysteresis loop

3.4 Results and Discussion

Figure 14 and Figure 15 show a pair of typical calculated results. Qualitatively, the expected hysteric behavior is exhibited.

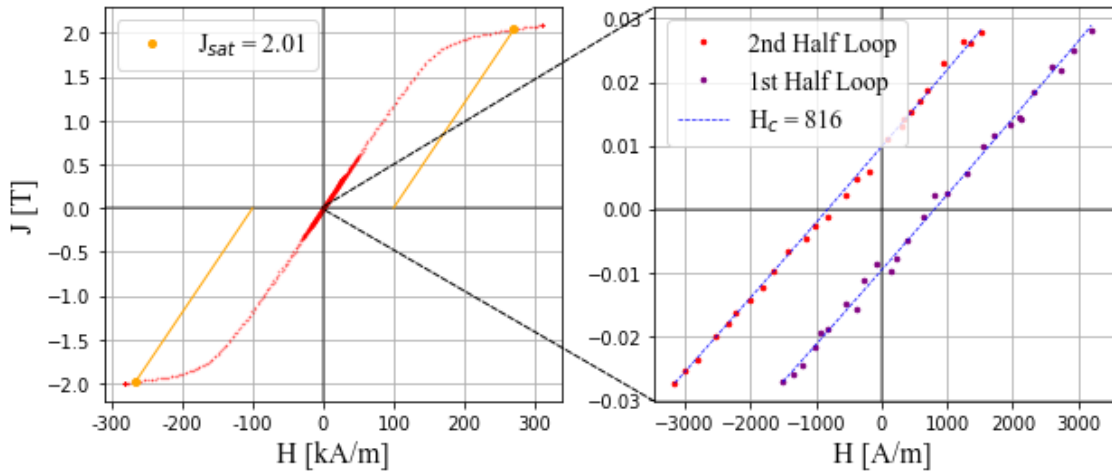


Figure 14: Typical magnetic hysteresis loop measured by the proposed instrument, with high saturation and coercivity. The orange lines represents a constant H_{eff} at H_{ref} , used to estimate J_{sat} while compensating for shape demagnification effects.

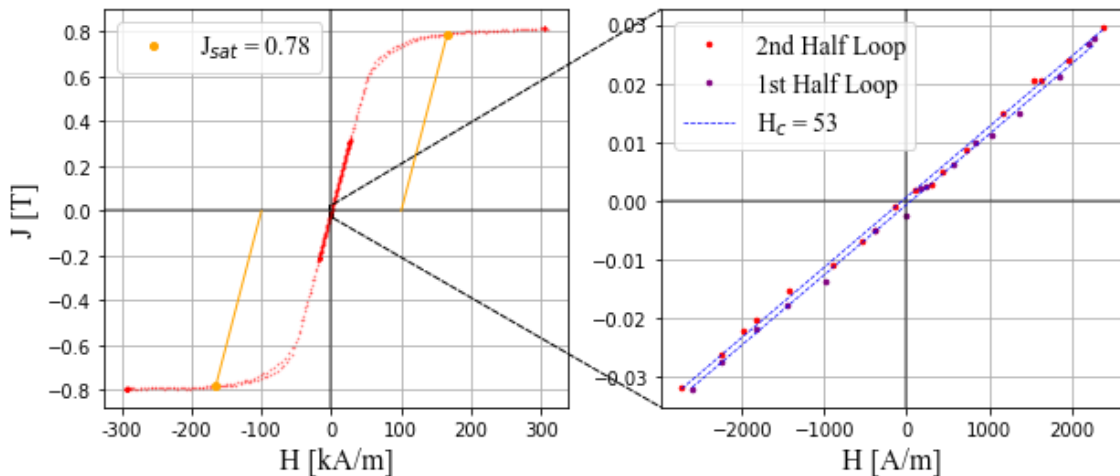


Figure 15: Typical magnetic hysteresis loop measured by instrument with low saturation and low coercivity. This specimen has lower shape demagnification factor N compared to Figure 14 as indicated by the greater slope of the orange line.

3.4.1 J_{sat} measurements accurate across wide range of values, approximately 1% relative errors when using constant reference field

The calibration required for calculating J_{sat} described in Implementation are performed using these 15 specimens. However, to assess the accuracy of J_{sat} it was necessary to calibrate individually for each specimen using only the other 14 specimens as cross-validation. Additionally, J_{sat} is calculated utilizing two different methods. The first is according to the actual maximum value of J achieved, which will be more accurate but not be completely comparable due to the greater magnetizing field of the VSM. The second method is approximating J_{sat} as described in 3.3.2.2 with $H_{ref} = 100kA/m$, which will be fully comparable. The maximum magnetic field $H_m \approx 500kA/m$ for the VSM is greater than for the proposed instrument ($\approx 100 - 250kA/m$ depending on shape demagnification factor); thus, using a constant reference to calculate $J_{sat} = J(H_{ref})$ will better indicate if the results agree.

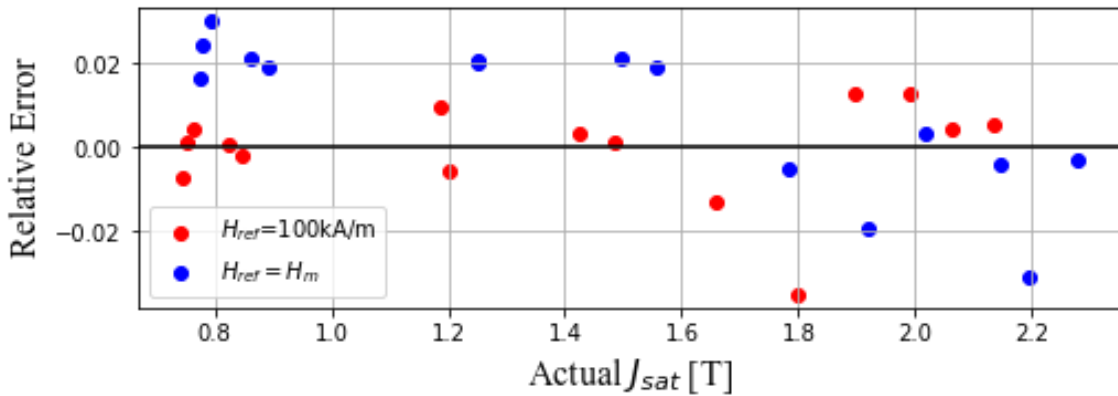


Figure 16: Error in J_{sat} measurements for graded Hipercos50/Hymu80 specimens compared to VSM. Two calculations of J_{sat} are shown: calculated as the maximum value of J at H_m , and at a common reference value H_{ref} of H_{eff} for comparability

The results in Figure 16 show agreement with VSM measurements across a wide variety of J_{sat} . When calculating J_{sat} at a fixed $H_{ref} = 100kA/m$, the Mean Average Percent Error (MAPE) is 1.1%, with a max error of 3.5%. If this is not fixed between both instruments, a bias can be observed where greater J_{sat} are underestimated. Because of the effect on the calculated flexure stiffnesses, this also results in an overestimate of lower J_{sat} . This bias at greater J_{sat} is due to the greater fields achieved with VSM achieving more complete saturation for the more difficult to magnetize specimens. All specimen with $J_{sat} < 1.6T$ were likely fully saturated and would thus still be accurate otherwise. Designing specimen to have a low shape demagnification factor N can also ensure that full saturation is achieved.

3.4.2 *Coercivity repeatable to 20-30A/m, with greater accuracy. Shape biases minimal*

For the 3 specimens cut from the Fe6Si ring specimen, a limit of $\delta = 0.03T$ is used to select the points for fitting coercivity, based on $|J| < \delta$ as discussed 3.3.2.1. This threshold is used except where otherwise noted for all other subsequent measurements as well. The specimens were tested along their long axis, corresponding to the circumferential direction of the ring. In Table 3, it can be observed that differences in \overline{H}_c for the 3 geometries are small when compared to σ_{H_c} . The high and low values for H_c both differ from the median value by less than one standard error of the mean, considering the sample size, and with no apparent trend with aspect ratio. Thus, there is no apparent shape bias in H_c in these measurements. The results of the previous characterization of ring specimen that these specimens were cut from was that coercivity was 165A/m for one half loop and 190 A/m for other. The measured results are consistent with the lower value, recognizing

that the proposed instrument is unable to measure asymmetry in H_c . Repeatability for the 3 specimens was 20-30A/m. J_{sat} also shows low bias, and is highly repeatable, with 0.2% standard error or less for all 3 specimens. $\overline{J_{sat}}$ was approximately 2% greater for the 3rd sample; this could reflect bias, but also is consistent with the accuracy results from 3.4.1.

Table 3: Comparison of H_c, J_{sat} for different Fe-6Si Geometries (N=15, each)

Dimensions	$\overline{H_c}$	σ_{H_c}	$\overline{J_{sat}}$	$\sigma_{J_{sat}}$
4.39x3.85x1.80	162	20	1.0653	0.0006
4.07x3.84x1.86	169	33	1.0625	0.0007
3.90x3.89x1.84	158	22	1.0813	0.0015

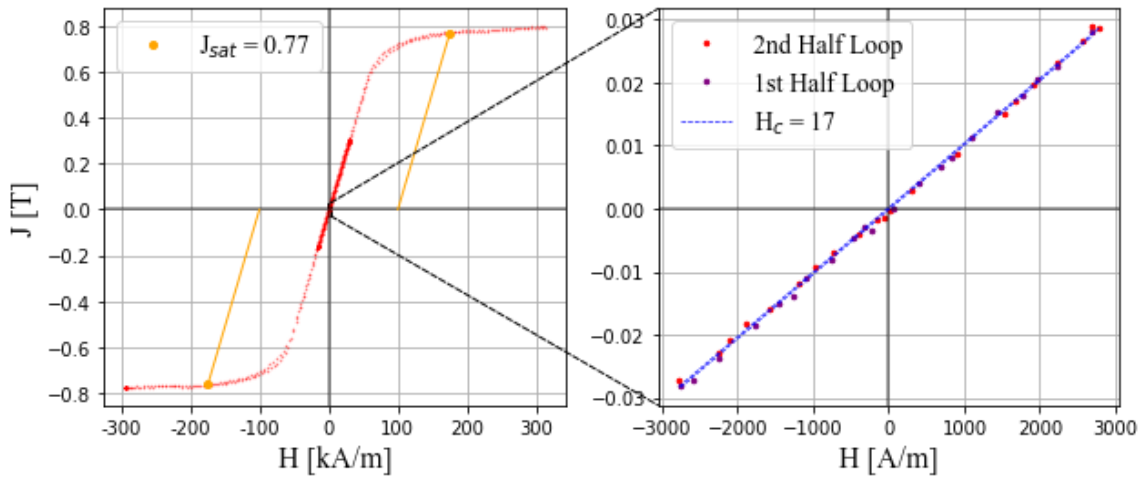


Figure 17: Magnetic hysteresis loop for wrought Permalloy, with expected $H_c \approx 0$

Figure 17 shows one of the results for measuring the wrought Permalloy specimen. 10 measurements were made, resulting in a $\overline{H_c} = 0.3$ and $\sigma_{H_c} = 18$ A/m. Thus, there is no measurable bias, at least for low H_c . Repeatability is similar to the prior set of the results.

To check repeatability at higher H_c , one of the specimens from 3.4.1 with $H_c \sim 900$ A/m was measured 10 times. This resulted in a $\overline{H_c} = 863$ and $\sigma_{H_c} = 78$ A/m. Because J_{sat} was high (~ 2 T) for this specimen, the number of points fitted for coercivity compared to the previous measurements where $J_{sat} < 1$ T was lesser. If instead $\delta = 0.06$ T

is used to select points for fitting coercivity, these results change to $\overline{H_c} = 876$ and $\sigma_{H_c} = 62$ A/m. Further using $\delta = 0.2T$, $\overline{H_c} = 874$ and $\sigma_{H_c} = 34$ A/m. Thus, uncertainties may increase relative to the coercivity, but this can be largely mitigated by increasing δ with minimal impact on accuracy.

3.4.3 Applicable to as-built AM specimens with poor form

Table 4: Repeatability of H_c, J_{sat} for 6 Similar AM Permalloy Specimens

SPECIMEN	1	2	3	4	5	6	σ
J_{sat} [T]	0.693	0.705	0.692	0.689	0.696	0.693	0.005
MASS MAG. [Am^2/kg]	78.2	78.6	78.4	79.5	78.0	78.9	0.5
H_c [A/m]	146	196	149	134	155	223	32

Table 4 shows magnetization results are highly repeatable even for as-built specimen, on both a volume basis (J_{sat}) and on a mass basis, with <1% relative errors. This is less repeatable than prior results, though this could reflect intrinsic variability in the process used to manufacture these specimens. H_c however, has comparable repeatability to prior results.

3.4.4 Application to data-intensive measurements demonstrated

To demonstrate the high rate of measurement possible, we also measured First-Order Reversal Curves (FORC) of one of the specimen included in Figure 16. 10 reversals could be conducted in merely 56 seconds (Figure 18).

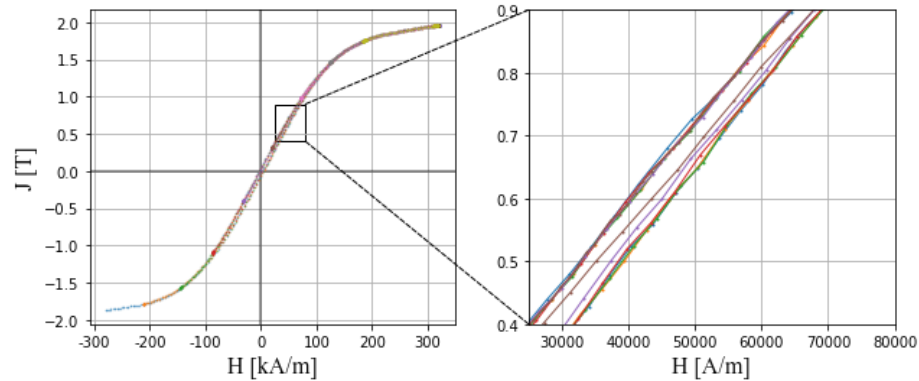


Figure 18: First-Order Reversal Curve of AM specimen. The specimen had a full loop coercivity of approximately 3000 A/m.

3.5 Conclusion

From these test results on a wide variety of AM and wrought samples, it is found that a complete magnetic hysteresis loop can be measured in under 20 seconds, with minimal setup or calibration time. This throughput is only limited by the sampling rate of the measurements, and represents a significant improvement compared to existing capabilities which often take many minutes. Accuracy and repeatability were assessed; magnetization was generally accurate to $\pm 1\%$, comparable to many existing high-fidelity instruments, and highly repeatable as well, as low as 0.2%. Coercivity was found to have greater uncertainties but was generally repeatable to 20-30 A/m. This is significantly inferior to existing high-fidelity measurements but will in most circumstances be sufficient for the applications of screening and exploration. The order of magnitude reduction in cost and high-throughput make this instrument a desirable option where the fidelity is acceptable, and represents a unique set of tradeoffs compared to existing options. Possible further improvements are discussed in 5.2.1. One possible extension of this device is to

allow common rotations of the pair of permanent magnets about the specimen, which would allow 3D magnetization histories to be achieved, another major advantages to use.

CHAPTER 4. PROCESS OPTIMIZATION OF THE ELECTRON BEAM POWDER BED FUSION OF PERMALLOY

4.1 Introduction

Metal Additive Manufacturing (AM) has come to encompass an increasingly diverse set of processes, applications, and materials. Materials difficult to process with conventional methods can often be successfully developed with AM. For some alloys, new geometries can be manufactured that would be otherwise costly or impractical [4]. AM processes also have many factors that can be controlled on-demand, creating significant opportunities for optimization and process development. AM solidification dynamics with very high cooling rates can achieve superior properties to wrought materials. Advanced scan strategies can also be manipulated to spatially control microstructure, allowing further improvements. AM also poses many challenges, however. Defects and various process instabilities are prevalent, and large feature spaces can be difficult to adequately explore. AM processes can also be very sensitive to cofactors and difficult to qualify, which poses a major challenge to industry adoption [34].

Electrical machinery is one application of AM that has seen increasing attention in recent years. Stacked laminations are ubiquitous, yet these are time consuming and expensive to assemble. Additively manufactured alternatives have the potential to reduce manufacturing time by 40% [16]. Optimized geometry and localized manipulation of microstructure or composition can further enable new opportunities for more efficient or cost-effective electrical machinery. Many magnetic materials have poor mechanical

properties, which has its own impacts on performance and cost; some works have been able to take existing magnetic alloys and dramatically improve mechanical properties with AM. Babuska et al., for example, were able to achieve highly ductility with Hiperco printed by Laser Beam Powder Bed Fusion (PBF-LB), compared to conventional wrought properties [35].

Electron Beam Powder Bed Fusion (PBF-EB) is an AM technique that has seen increasing application to the manufacturing of electrical machinery. On account of being a hot process, PBF-EB can result in lower distortion and residual stresses than other AM processes. Additionally, electron beams can be deflected near instantaneously, allowing for more complex scanning patterns of the electron beam. Quasi-beam strategies utilize a single beam to melt multiple areas at once, which has been found to improve surface condition [21]. It is also possible to scan in a grid of discrete points rather than lines. In Plotkowski et al. (2021), the order in which a grid of point is scanned is manipulated to control microstructural texture [36]. These aspects of PBF-EB have made it an attractive method for manufacturing electrical machinery. Low distortions may enable printing of intricate thin walls, while the high temperatures may act similarly to heat treatments which achieve ideal magnetic properties by coarsening microstructure. Coercivities achieved however are typically greater than wrought values, often in the range of 100-1000 A/m. Silicon Steel printed by PBF-EB, for example, was able to achieve dense parts with a coercivity of 319 A/m [37].

Permalloy is a high-performance soft magnetic alloy widely used in industry. While it has not yet been printed with PBF-EB, Permalloy has been printed with PBF-LB and welded with Electron Beam welding [38]. Mikler et al. were able to achieve a H_c of 4.9

Oersted (390 A/m) with PBF-LB. This remains significantly higher than typical wrought values, for which $H_c < 1 A/m$ can be achieved with heat treatment.

To explore a large feature space including possible advanced scan strategies, we focus on high-throughput phenomenological screening techniques. This includes the characterization of magnetic properties as developed in CHAPTER 3, along with high-throughput methods for measuring density and surface condition. Our objective is to demonstrate the combination of high-throughput techniques, screen for a stable process window, and investigate possible effects of advanced scan strategies for future research.

4.2 Materials and Methods

4.2.1 Specimen Manufacture via Electron Beam Power Bed Fusion

4.2.1.1 Powder Material and Methodology

Permalloy powder with a given size distribution of $-106\mu\text{m}/+45\mu\text{m}$ was acquired from *Sandvik Osprey* [39]. The powder was manufactured by gas atomization in a Nitrogen atmosphere. Table 5 shows the reported composition. The tap density (per in-house *Sandvik Osprey* method based on ISO 3953) was also reported to be $5.2 g/cm^3$; this refers to density reflecting the packing efficiency after mechanical tapping.

Table 5: Measured Composition of Fe80Ni4Mo Powder, per Supplier

Element	Ni	Mo	Mn	Si	O	C	P	S	N	Fe
Wt %	79.7	4.1	0.34	0.12	0.02	0.01	0.01	0.003	0.00	Bal.

The virgin powder's density was measured using an AccuPyc II Gas Displacement Pycnometry System, with Helium analysis gas. Powder was also inspected with Phenom

XL G2 SEM. Powder size distribution was measured with a Malvern Mastersizer 3000 by laser diffraction.

For PBF and many other AM Processes, it is necessary to consider the lifetime of the powder. The following sequence was followed:

1. Virgin powder is loaded into the powder hopper
2. After a print, powder from the spillover bins is emptied into a separate “used” powder canister
3. Large, heavily sintered chunks of powder are removed from the build plate and bedding powder (see Figure 5), and are also added to the “used” powder canister
4. The “used” powder is tumbled for several hours in a mixer to break apart heavily sintered conglomerations of powder
5. The broken down “used” powder is added back to the bedding powder such that there is 30mm of powder below the build plate

4.2.1.2 Printer Operation and Specimen Design

Table 6: Printer Characteristics

Printer	<i>Freemelt ONE</i>
Accelerating Voltage	60 <i>kV</i>
Cathode	LaB ₆
Cathode Heater	CO ₂ Laser
Max Chamber Vacuum	10E-6 <i>mbar</i>

Specimens were printed using the Freemelt ONE PBF-EB system, the characteristics of which are shown in Table 6. The nominal specimen geometry was a 3x3x3mm cube. The arrangement of specimens on a build plate is shown in Figure 19. The total number of specimens varied, as it was feasible to print more at lower energy densities,

but was typically around 50. An additional 6 or more specimens were used for process monitoring and kept constant every print.

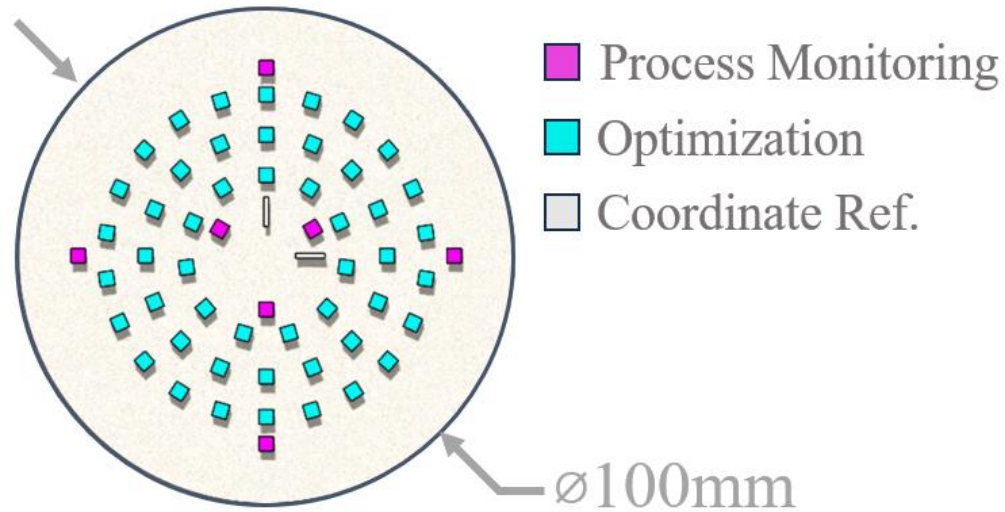


Figure 19: The organization of build plate. Specimens designated for process optimization are arranged evenly in an annular region. These specimens are bounded on the inside and outside by a total of 6+ specimens designated for the purpose of process monitoring. Finally, two single-track line scans provide a set of coordinate axes for reference.

A major bottleneck in additive manufacturing is the removal of specimens from the build plate, such as by Electrical Discharging Machining (EDM). We implement an architected break, such that specimen can be removed by hand or with simple tools and immediately placed into indexed storage. This is accomplished by intentionally weakening a set of layers, as is shown Figure 20. This has the added benefit of giving greater time for the process to stabilize before contributing to the specimen. Adjustments had to be made to the number of weakened layers over time, as greater energy densities resulted in deeper melt pools. These changes were tracked and considered in process monitoring in case there was any resulting effect on properties.



Figure 20: Architecture of break-off specimens. 10 layers are printed at an energy density of 0.8 J/mm^2 to ensure fusion to the build plate and accommodate any initial settling of the build plate. Subsequently, 25 layers are printed at energy density varying progressively from 0.4 J/mm^2 to 0.3 J/mm^2 . Finally, the 60 layers with the intended factors are printed. The melt pools from these can extend well into breakoff section, as can be seen above.

4.2.1.3 Scan Strategy and Featurization

6 factors were used, overviewed in Figure 21. These are: *scan*, *energy density*, *power*, *hatch*, *layer-to-layer rotation*, and *step*. *Scan* includes two different types of scans: line scans, and “dot scans,” consisting of a grid discrete point.

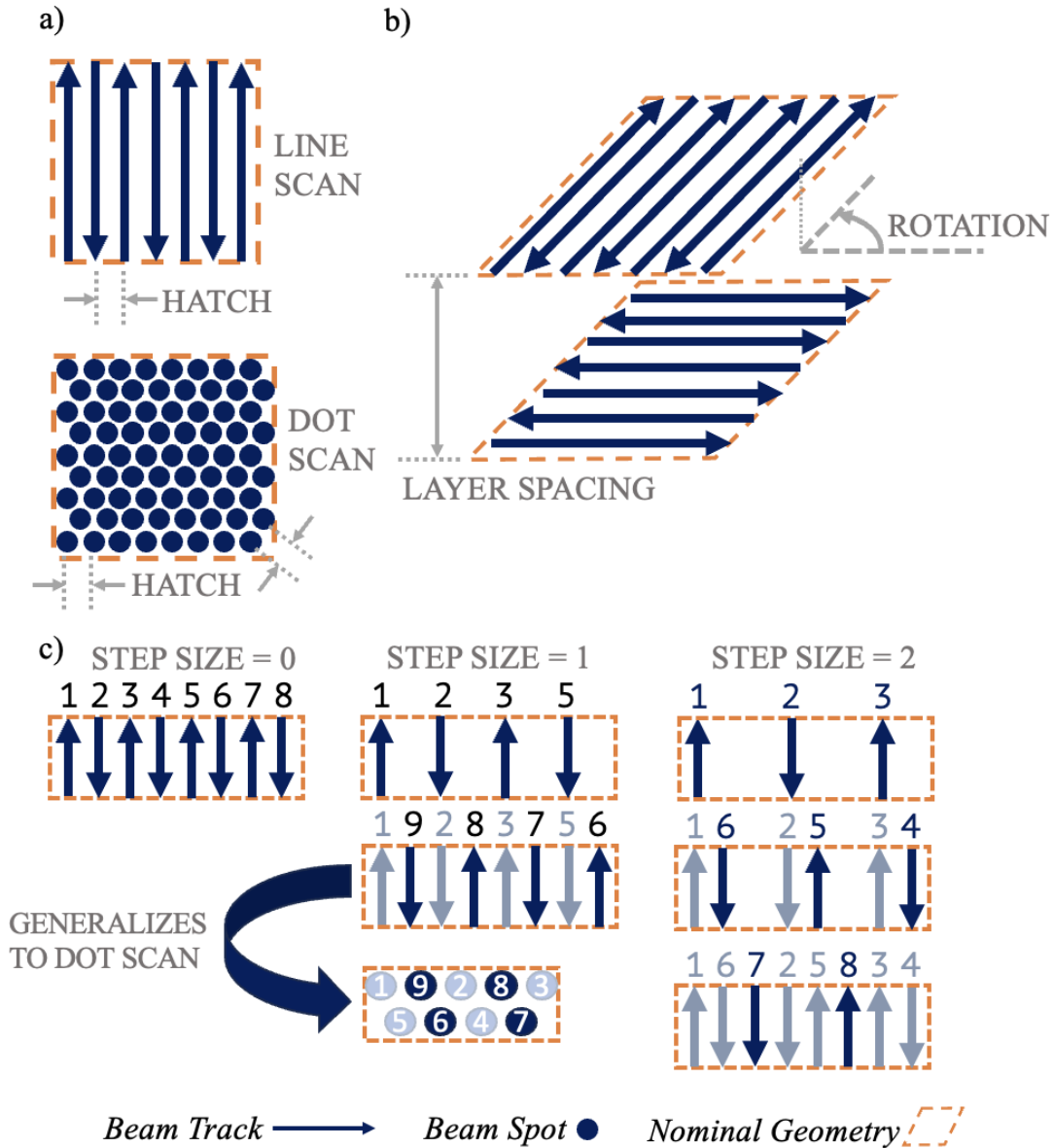


Figure 21: Different scan strategies and their featurization. a) “Scan” can be either “line” or “dot,” as either a set of parallel lines or grid of point scans, respectively. “Hatch” determines the spacing of adjacent lines/dots. b) Layer-to-layer “rotation” and layer spacing. c) “Step” determines order according to the gap between sequential lines/dots, effectively creating multiple passes.

Energy Density is defined as follows:

$$ED_{line} = \frac{P}{vh} \tag{11}$$

$$ED_{dot} = \frac{\sqrt{3} Pt}{2 h^2} \quad (12)$$

where P is beam power, v is beam speed, h is hatch, t is dwell time (per point). Equation 11 and 12 can be used to calculate the speed of the beam from *Energy Density* and other factors. *Step* is motivated by the possible advantages of quasi-beam patterning.

Table 7 shows the domain of different factors, along with the value used for the reference samples shown in Figure 19. Because of machine limitations preventing arbitrary choice of power (see 4.2.4.2 for further discussion), the power used for this reference sample could not always be constant but was guaranteed to be from within a narrow range.

Table 7: Electron Beam Powder Bed Fusion Factors

Factor	Values	Value, Reference Specimen	
Scan Strategy (“Scan”)	<i>(Scan, Line)</i>	<i>Line</i>	
Beam Power (“Power”)	[250, 1000]	[850, 1000]	<i>W</i>
Energy Density (“ED”)	[0.5, 9.5]	0.7	<i>J/mm²</i>
Hatch	[75, 200]	100	<i>μm</i>
Rotation	(0, 90, 180)	0	<i>°</i>
Step	(0, 1, 2, 3)	0	

In addition to these factors, numerous other parameters were isolated as co-factors, based on prior art and initial screening experiments. These generally are parameters that must be kept constant across a build plate, and thus would be impractical for high-throughput exploration. These co-factors are shown in Table 8. Because of the Freemelt ONE’s open loop heating control, preheat temperature could not be constant across all experiments but instead was successfully kept within a narrow range by analytically chosen preheat times.

Table 8: Electron Beam Powder Bed Fusion Co-factors

Co-Factor	Value
Layer spacing	50 μm
Powder Feed per Layer	75 μm
Preheat Temperature	850 ± 20 $^{\circ}C$
Preheat Power	1000 W
Preheat Time	30 ± 2 s
Recoater Speed	200 mm/s
Build Plate	<i>Carbon Steel, Ground and Sandblasted</i>

The Freemelt ONE does not have a dedicated slicer, and furthermore uses the open-source “.OBP” machine code format. A custom slicer was developed to achieve the desired scans shown in Figure 21.

4.2.2 Characterization

Four primary measurements were taken: density, surface roughness, saturation magnetization, and coercivity. Before removal from the build-plate, surface roughness of the top surface of the specimens was measured using the Keyence VR-3200 3D profiler. Sa (arithmetical mean height) according to ISO 25178-2:2012 was used to quantify surface roughness, itself used as a representative of surface condition. Specimen were then snapped off the build plates, with any loose material removed and wiped off with a dry Kimwipe. Archimedes density measurements were completed on a Mettler Toledo XSR104 Analytical Balance utilizing oil impregnation according to ASTM B962-17. Saturation magnetization and coercivity were measured utilizing the custom instrumentation developed in CHAPTER 3. Select specimen were sectioned with a diamond saw, and then progressively polished to 1200 grit by Silicon Carbide on a Pace NANO-1000s grinder-

polisher. These sections were then imaged with a Zeiss Axio Observer Z1 optical microscope.

4.2.3 *Experimental Design*

As applicable, the following sequence was followed to guide experiments:

- 1. Perform factorial experiments to find initial stable process window, downselect features, and determine cofactors.** During initial experiments, repeatability is not guaranteed as the process is adjusted and cofactors determined. Simple factorial designs allow conclusions to be drawn with a minimal number of comparable samples.
- 2. Sample initial feature space using Latin Hypercube Sampling (LHS).** LHS or another pseudo-random sampling method efficiently samples the feature space and creates an initial dataset that can train a Machine Learning (ML) model.
- 3. Suggest a batch of new experiments, interpolating within the feature space, using Active Learning where possible.** Active Learning enables the autonomous determination of new experiments according to an objective such as exploration or exploitation. For a 6-dimensional feature space efficiently choosing points may otherwise be challenging.
- 4. Expand feature space with new LHS samplings.** In case it is determined that the initial feature space is not comprehensive, the feature space can be expanded by sampling a new region with LHS. These new regions to sample are chosen according to domain expertise and best judgement.

4.2.4 Active Learning

Bayesian Optimization (BO) utilizing Gaussian Process Regression (GPR) is chosen as the Active Learning model. BO was implemented using the Python *bayesian-optimization* package. A Radial Basis Function (RBF) plus white noise kernel was chosen for GPR. The white noise component is used to capture the intrinsic variability in an AM process. The RBF is a reasonable choice for a physical process with non-periodic response.

4.2.4.1 Acquisition Function

To suggest new experiments, an acquisition function scoring the value of new datapoints is required. Expected improvement (EI) is equal to the expected value of the increase in maximum value from a new sample. In this work it is calculated as follows:

$$EI(x) = (\mu(x) - y_{max} - \kappa) + CDF(z) + \sigma(x)PDF(z) \quad (13)$$

$$z = \frac{(\mu(x) - y_{max} - \xi)}{\sigma(x)} \quad (14)$$

where *CDF* and *PDF* are the density functions of the normal distribution, $\mu(x)$ and $\sigma(x)$ are the predicted mean and standard deviation of $f(x)$, y_{max} is the max value seen so far, and κ is a hyperparameter. EI is chosen as an acquisition function as it can be utilized for either exploration or exploitation, depending on the hyperparameter κ , with $\kappa > 0$ biasing the results towards exploration.

4.2.4.2 Batch Selection

For a batch of specimens to be printed on a given plate, there are certain constraints. This includes factors that must be constant for the entire print. Some of these have been successfully isolated as cofactors, such as layer height. However, *power* could not be excluded and imposes significant constraints on operation. It takes a few seconds to change the power of the beam to a stable value, as can be seen in Figure 22.

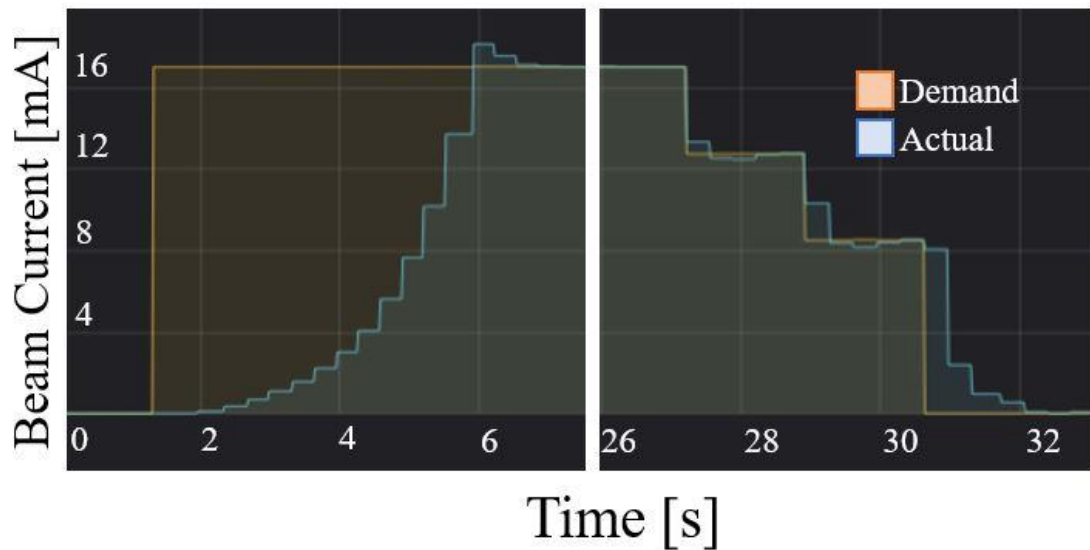


Figure 22: Set power (orange) vs. actual power (blue). One can observe it takes approximately 5 seconds to achieve steady state when ramping up, and approximately 2 seconds when ramping down.

Consequently, it is only practical to have 2-3 different power levels in a single print. Different approaches were taken to determine these, but most commonly 3 power levels were selected in descending order according to:

- $(850 + x/2) W$
- $(550 + x) W$
- $(550 - x) W$

where $x \in [0,300]$.

Thus, each batch, three different power levels are used, except in the edge case of $(850W, 550W)$. This strategy keeps the total heating of the plate similar print-to-print by combining lower powers with higher powers. To select a set of powers for a batch, the different possible sets of power are iterated over, to find which one results in the greatest Expected Improvement (EI), when summed over the entire batch. For a given set of powers, the total EI is calculated as follows:

Up to the total number of points in a batch:

- 1. At each power level, suggest a point and calculate its EI*
- 2. Pick the point with greatest EI, and add to the total EI so far*
- 3. Register the expected value of the point in model*

Thus, a batch of specimens can be chosen along with the optimal set of powers.

4.3 Results

4.3.1 Powder Characteristics

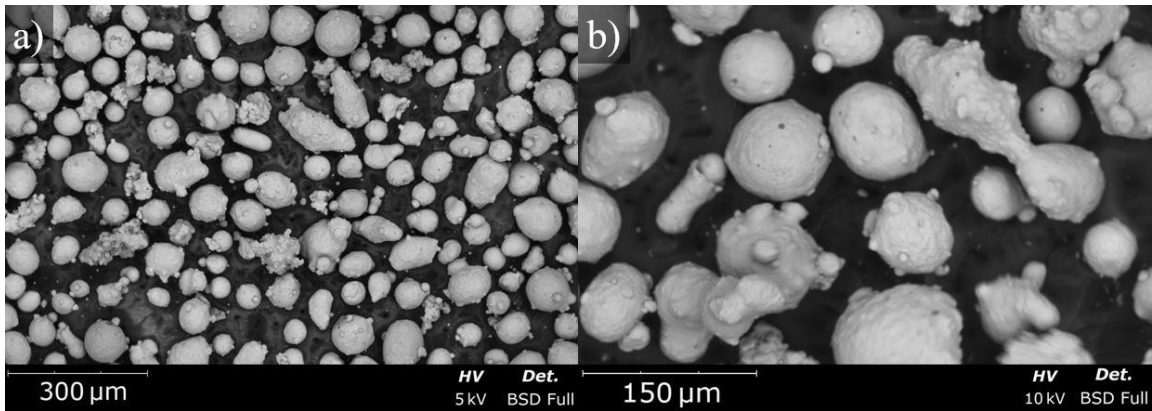


Figure 23: a) SEM image of as-received Permalloy Powder. Many particles are highly irregular, featuring a large aspect ratio or consisting of a conglomeration of smaller particles. b) Detail view showing several particularly irregular particles

Figure 23 shows SEM images of the virgin powder. Many particles are highly irregular, with high aspect ratios or even a dumbbell shape. Many particles are also covered in smaller nodules. Whether averaging over all particles or weighted by volume, the mean aspect ratio was approximately 0.75. Figure 24 shows the powder size distribution measured by SEM according to the circle equivalent diameter.

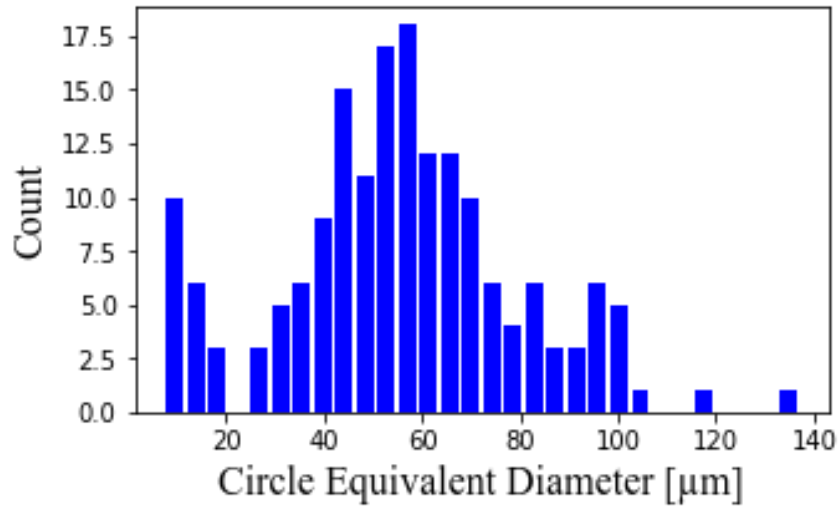


Figure 24: Powder Size Distribution, calculated from SEM image using circle equivalent diameter (N=174).

Powder size distribution measured by laser diffraction is shown in Table 9. A sample of the “used” bedding powder was also analyzed.

Table 9: Powder Size Distribution Percentiles

Powder Condition	D_{10}	D_{50}	D_{90}	
<i>Virgin</i>	49.9	74.8	111	μm
<i>Recycled Bedding Powder</i>	54.3	81.0	120	μm

The pyncometric density of the power was measured to be 8.64 g/cm^3 .

4.3.2 Printability

A major issue with PBF-EB is the risk of “smoke-out” events. It was found that these would reliably occur if the build plate temperature dropped below approximately 760°C (Figure 25). A preheating temperature of 850°C was investigated and found to give sufficient margins such that no smoke-out events would occur.

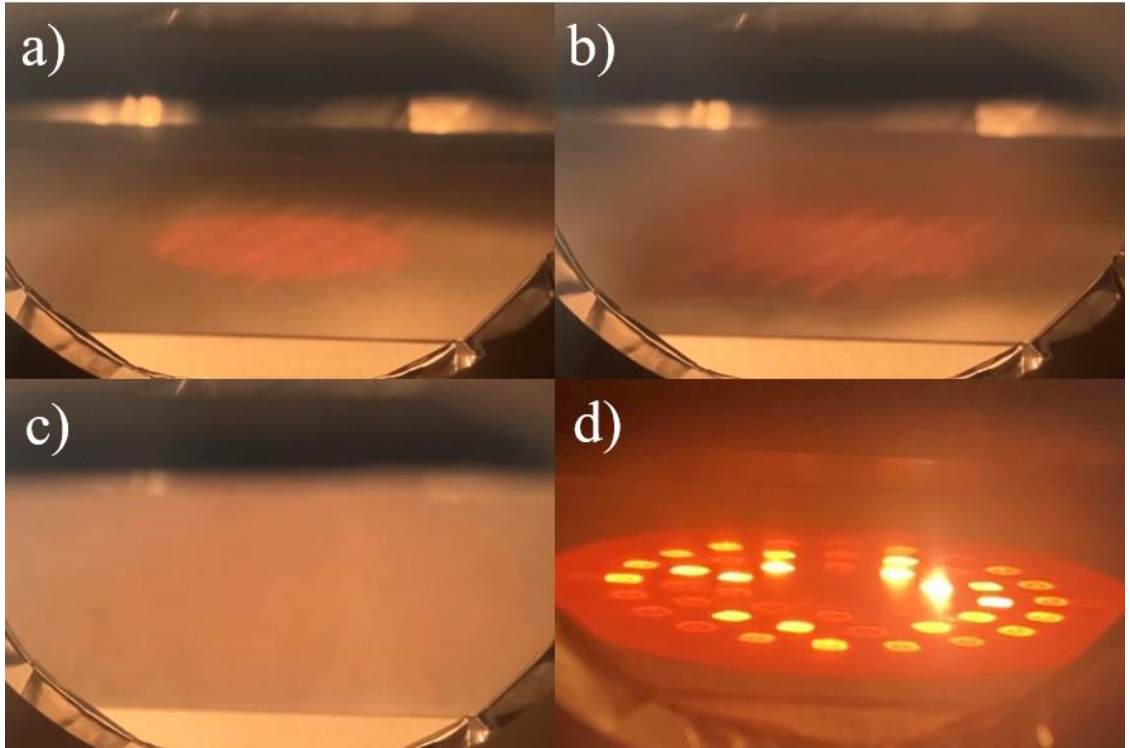


Figure 25: a-c) Progression of “smoke-out” event at 760°C. d) Nominal scanning at 850°C.



Figure 26: Transient cooling from 850°C after a completed print

4.3.3 Surface Condition

A variety of surface conditions were observed. At low energy densities, surfaces were non-smooth but without gross distortions. At high energy densities, some specimen became flat topped, while others showed severe balling which could create significant surface anomalies. Many examples of these can be seen in the two build plates shown in Figure 27.

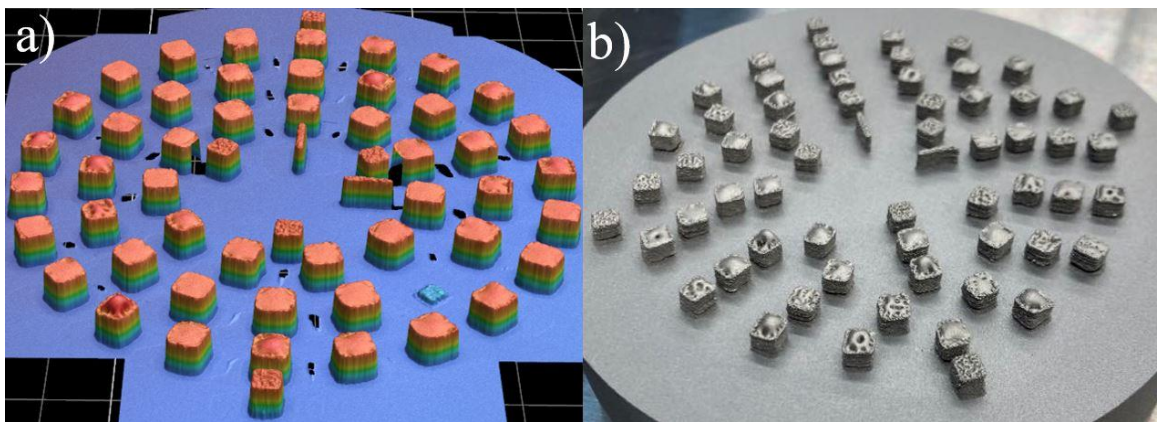


Figure 27: a) 3D measurement, from Keyence VR-3200. b) Picture of typical print, showing specimens with a variety of different surface conditions post-sandblasting.

GPR was unable to be successfully trained using the surface roughness response (Figure 28). Instead, results were analyzed by inspection. $250\mu m$ Sa was adopted as the threshold between “Poor” and “Acceptable” surface condition. Specimens above this value typically have bulging or warped surfaced. This could even cause damage to the recoater blades or disrupt prints. Based on this threshold, the total results are plotted Figure 30 relative to 4 of the 6 factors. Simple convex regions are used to classify the response.

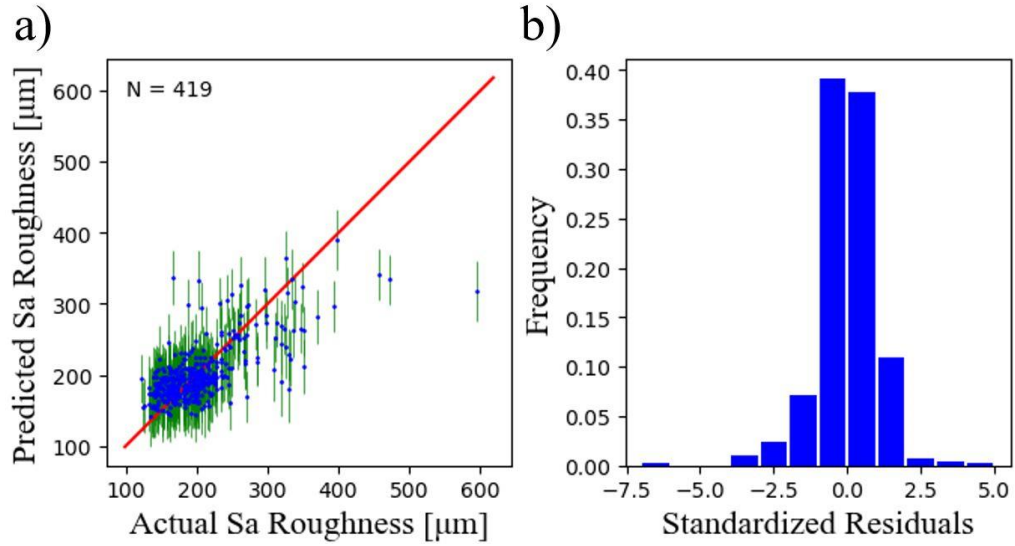


Figure 28: Surface Roughness parity plot, utilizing Leave-One-Out Cross-Validation (LOOCV). GPR is clearly unable to model this response. Likely this is a result of roughness being subject to threshold effects and thus not behaving representative of a Gaussian process as the model presumes.

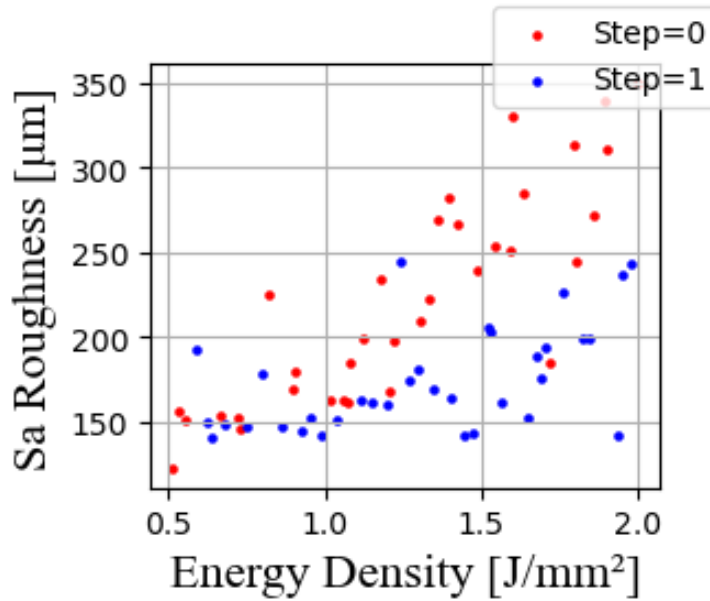


Figure 29: Results from a single LHS print. Regardless of all other factors, a step size of 1 reduces surface roughness (Sa) growth with energy density from up to 350 μm to below 250 μm

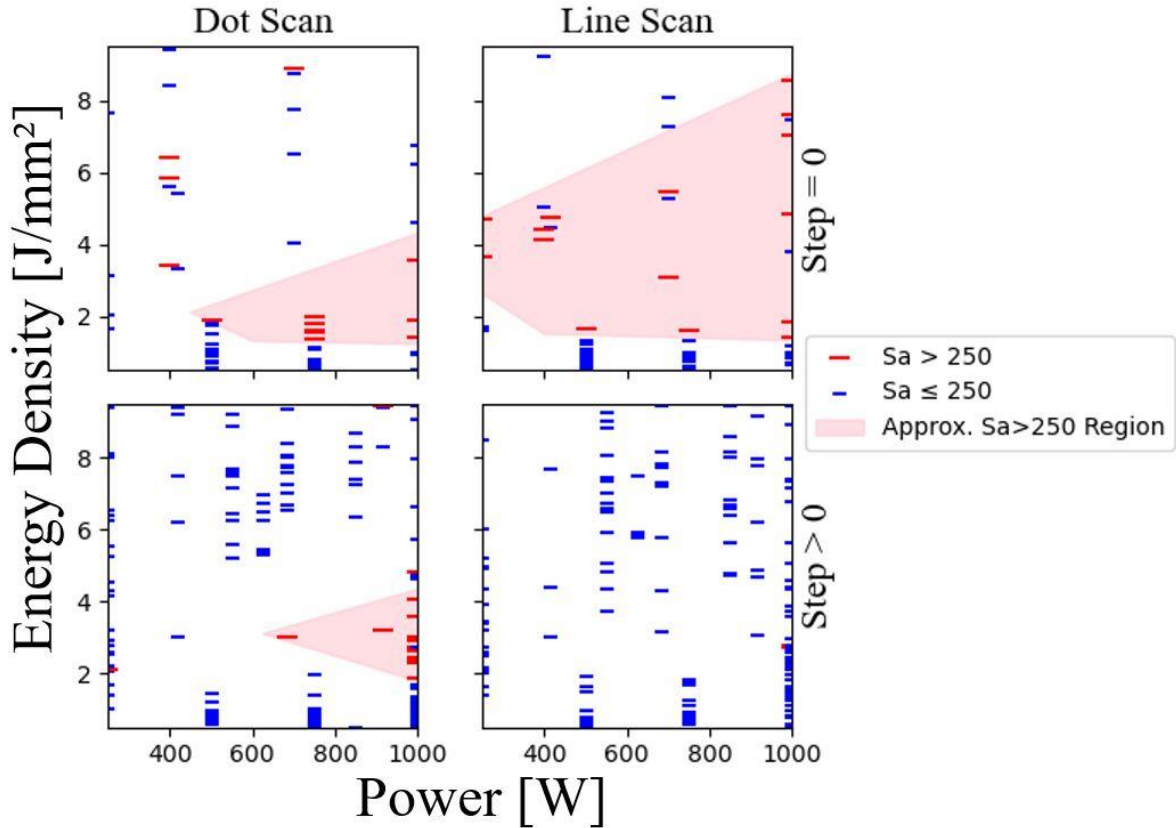


Figure 30: Surface roughness results, classified as poor/acceptable based on if the Sa surface roughness is greater than $250\mu\text{m}$. Convex regions are used to approximate the regions where poor surface condition is expected.

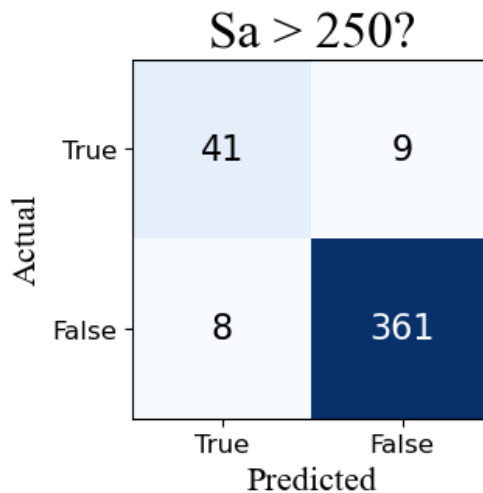


Figure 31: Confusion matrix for classifying surface condition. The practicalities of avoiding recoater damage limited the number of true positives which could be sampled.

4.3.4 Density

Unlike surface roughness, modelling with GPR was successful, enabling the employment of Bayesian Optimization. Many specimens for the purpose of density measurement were thus autonomously selected. Initial LHS experiments still oversampled lower energy densities, however. A parity plot for this model is shown Figure 32. Two factors, *Energy Density* and *Power*, predicted the entirety of the response except for a maximum effect of 0.06 g/cm^3 . This enables the predictions and actual values to be plotted on two axes (Figure 33). Most of the remaining variation is explained by *step*, shown in Figure 34.

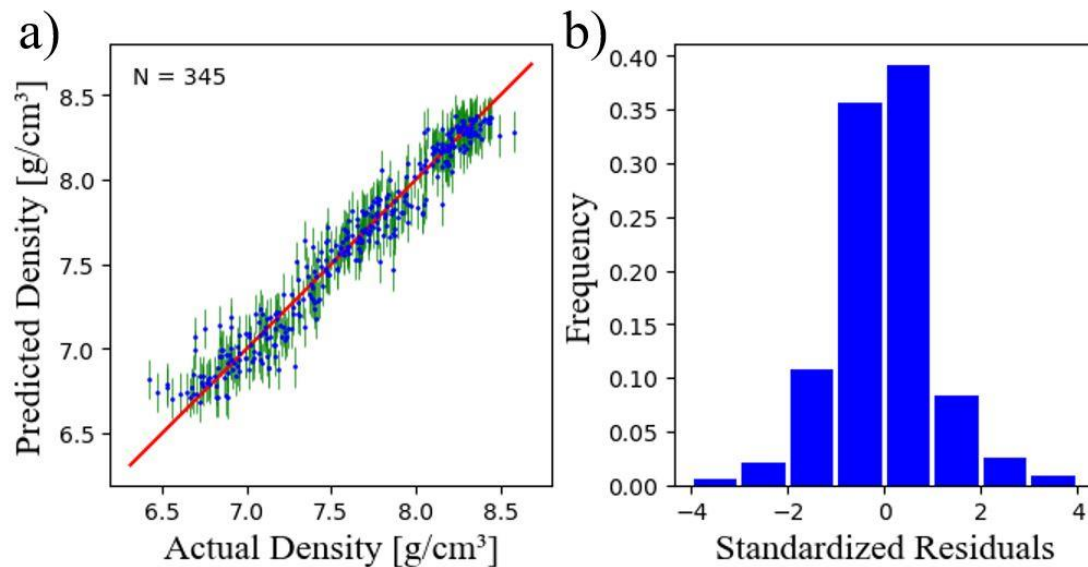


Figure 32: Cross Validation of GPR trained on Archimedes density. Some clustering of residuals can be visible, such as at the lower "tail" of overestimated densities. Overall, the residuals are well behaved and indicate a successful fit of the model. The clustering that is present can in part be explained by print-to-print variation.

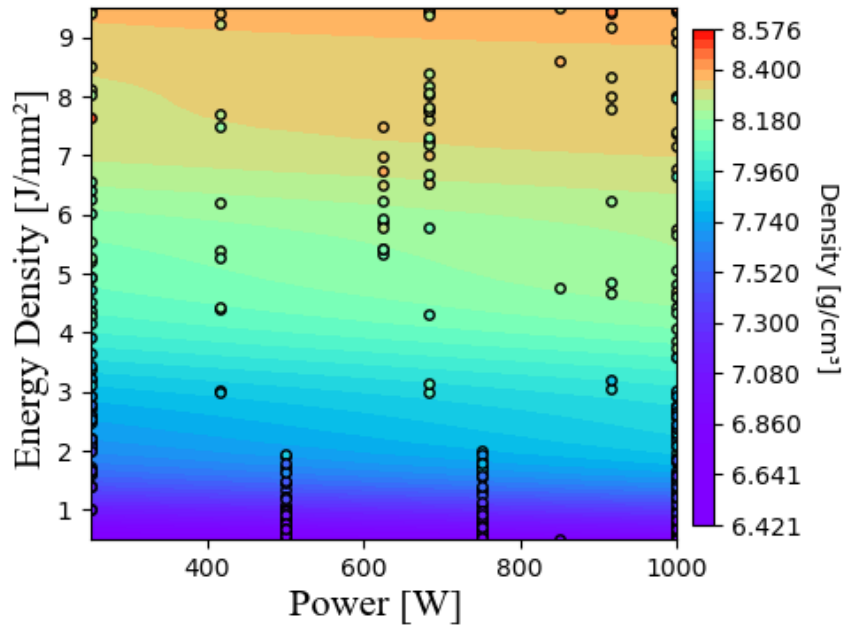


Figure 33: Best predicted densities by GPR, along with individual data points. The other 4 factors have minimal impact on density. A clear trend can be seen as Energy Density and to a lesser extent, power, increase density.

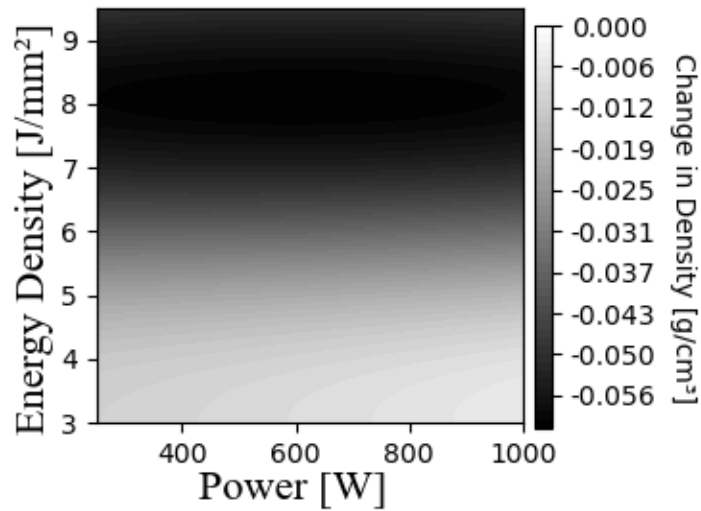


Figure 34: Change in density due to *step* = 3 vs. *step* = 0, for ED. It can be seen at higher energy densities, larger *step* has a slight negative impact on density.

4.3.5 Mass Magnetization

Because saturation magnetization is a volume basis measurement, it will be directly affected by the density; specimens with low density are certain to have poor saturation magnetization. However, it is also useful to separate any change in solid material properties vs. the effect of increasing density. Thus, we compromise by only considering specimens with density greater than 8 g/cm^3 , but calculate mass magnetization as a response instead of saturation magnetization. Mass magnetization is a comparable measurement, but on a mass basis instead of volume. A 1st order effect test was done for this response with regard to all 6 factors, the results of which are shown in Table 10. *Step* and *rotation* are treated as ordinal features, while *scan* is treated as a nominal feature. As the most significant effect, mass magnetization vs. energy density alone is plotted in Figure 35.

Table 10: First order effect test for least-squares regression of mass magnetization

<i>Term</i>	<i>Scaled Estimate</i>	<i>Standard Error</i>	<i>t Ratio</i>	<i>prob > t </i>
<i>Intercept</i>	76.259	0.239	318.57	<0.001
<i>Scan[dot]</i>	-0.041	0.036	-1.14	0.259
<i>Scan[line]</i>	0.041	0.036	1.14	0.259
<i>Power</i>	-0.071	0.053	-1.34	0.183
<i>ED</i>	0.411	0.064	6.43	<0.001
<i>hatch</i>	0.006	0.046	0.12	0.9019
<i>Step[1-0]</i>	0.500	0.232	2.16	0.033
<i>Step[2-1]</i>	0.268	0.092	2.92	0.004
<i>Step[3-2]</i>	-0.183	0.095	-1.93	0.056
<i>Rot[90-0]</i>	0.042	0.087	0.49	0.626
<i>Rot[180-90]</i>	-0.009	0.085	-0.12	0.907

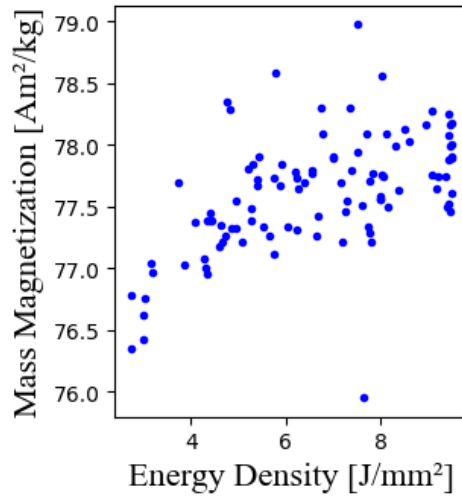


Figure 35: Mass Magnetization increases with Energy density (N=102)

4.3.6 Coercivity

No trends were observed in coercivity, but the distribution of measured values from a single print are shown in Figure 36. Given the variability in the measurement, it is likely that coercivity was generally between 150-200 A/m.

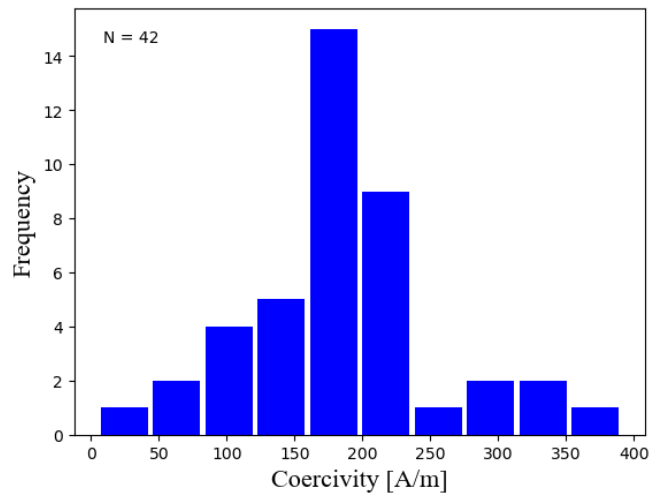


Figure 36: Distribution of measured coercivities from a single batch. No trends were found relating to the different factors.

4.3.7 Process Monitoring

As shown in Figure 19, on each print a set of reference specimens was printed for the purpose of process monitoring. Two possible sources of print-to-print variation are identified and recorded: changes made to the number of break-off layers, and variations in build plate temperature due to open-loop control. Figure 37 shows these results, which show print-to-print variation but no overall trends.

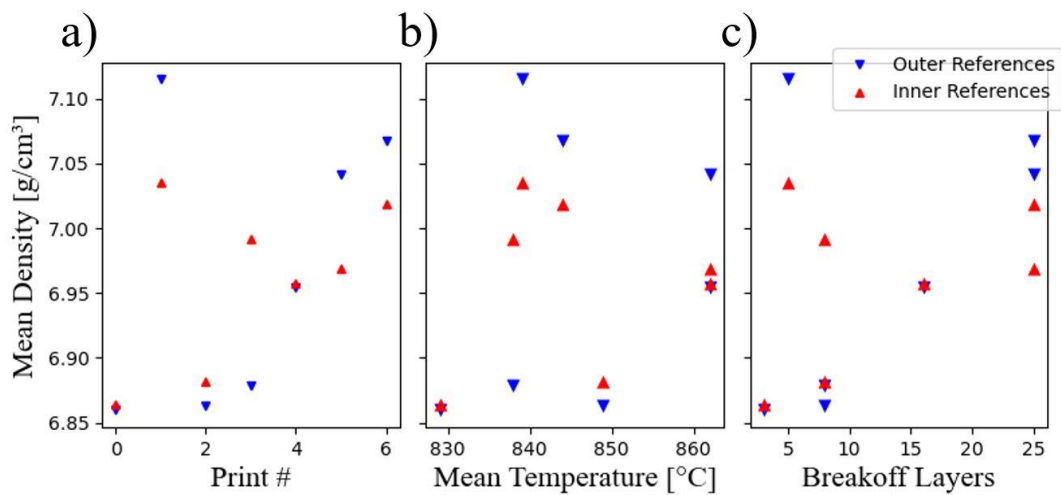


Figure 37: Results of process monitoring, considering two major possible cofactors of build plate temperature and the number of breakoff layers. “Inside” references are located near the center of the build plate, and “outside” references with the opposite definition are distinguished. While there is clear print-to-print variation, there is no apparent dependency on either of these cofactors or on the chronology.

4.3.8 *Microscopy and Microstructure Characterization*

Three specimens were selected at 3 different energy densities, to compare the measured Archimedes density and observed porosity. Two of these were at greater energy densities (4.7 and 9.5 J/mm²), which show nearly fully dense cores but exhibited porosity at the sides and bottom. The specimen printed with a low energy density of 3.0 J/mm² by contrast shows porosity and lack of fusion throughout the volume.

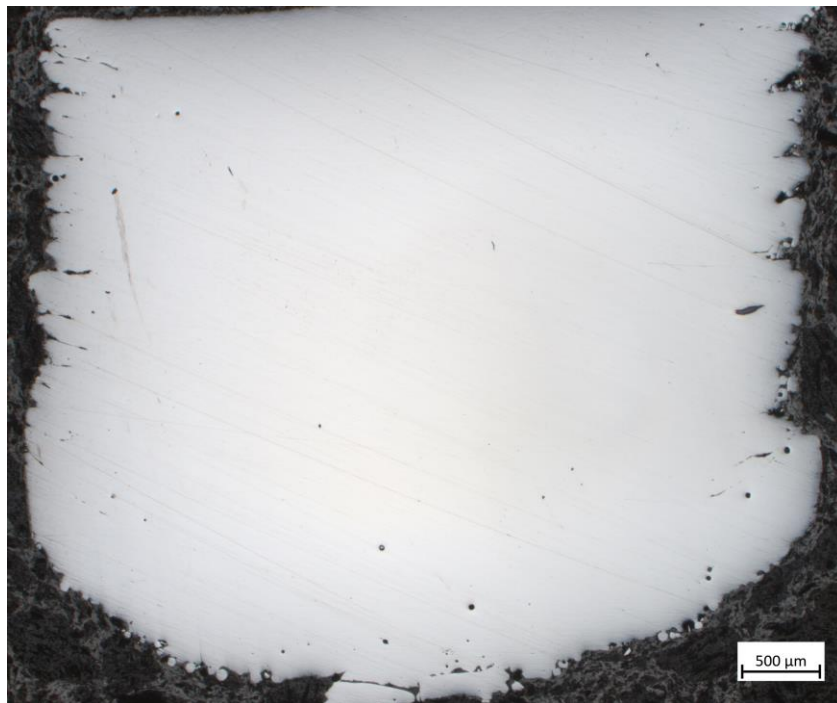


Figure 38: Cross section of specimen with ED of 9.5 J/mm² and Power of 917W. While the center is nearly fully dense, some pores and cavities exist at the sides and bottom.

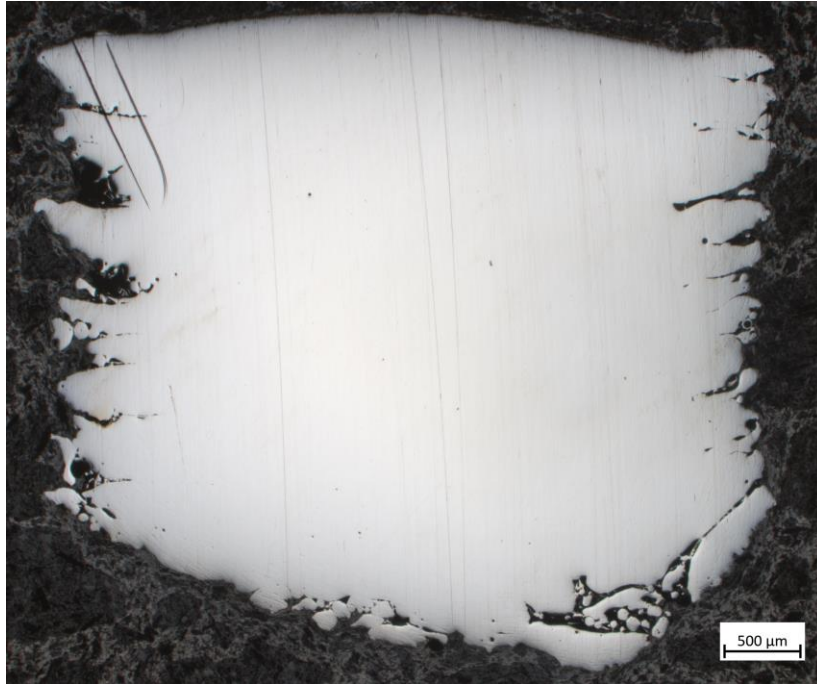


Figure 39: Cross section of specimen with ED of 4.9 J/mm² and Power of 917W. While the center is nearly fully dense, large pores and cavities exist at the sides and bottom.

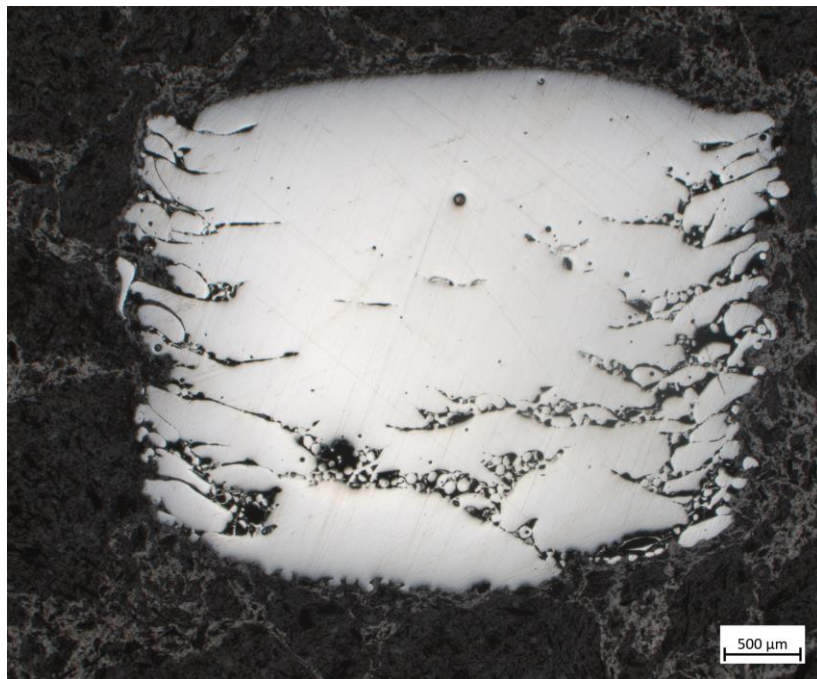


Figure 40: Cross section of specimen with ED of 3.0 J/mm² and power of 917W. Significant porosity and lack of fusion can be seen throughout the volume.

4.4 Discussion

4.4.1 *Sintered Powder can be Largely Broken Down*

The as-received powder was characterized to be a mix of spherical and non-spherical particles with a mean aspect ratio of approximately 0.75 (Figure 23). While the sample size is limited, the circle equivalent diameters shows good adherence to the upper sieve bound, a concentration towards the lower end of the distribution, and many particles below the lower sieve bound (Figure 24). It is possible that many of these smaller particles $<20\mu\text{m}$ could be nodules, either misidentified as separate particles or having passed through the sieve while still attached to larger particles.

From Table 9, we can conclude that the tumbling of powder was effective in breaking apart the sintered powder. Compared to virgin powder, the recovered powder only showed a marginal increase in distribution percentiles. D_{50} only increased from 74.8 to 81 μm , and D_{10} and D_{90} similarly increased by approximately 10%. This indicates that while some powder particles likely remain sintered together, most were successfully broken apart into near-individual particles. The chosen preheating temperature of 850°C thus only lightly sinters the powder, while still preventing the “smoke-out” instability.

4.4.2 *Surface Condition Highly Dependent on Four Factors Including “Quasi-Beam” Advanced Patterning Techniques*

Trends governing surface roughness became apparent upon inspection of the large dataset. The most critical feature effecting surface roughness was *step*, for which values greater than 0 created “quasi-beam” patterning where features are not scanned in order.

The positive importance of this technique agrees with prior art [21]. In the LHS shown in Figure 29, none of the $step > 0$ specimens have a surface roughness greater than $250 \mu m$, in contrast with the $step = 0$ specimens where this grew to nearly $350 \mu m$. The lower surface roughness in the former case demonstrates the effect of $step$ in controlling surface roughness. $Power$ and ED (which can be alternatively featurized in terms power and speed) are also well understood to control melt pool stability and govern the emergence of balling. Thus, it can be understood why all 4 of the factors included in Figure 30 were found to have importance.

For $step > 0$ and a *line* scan strategy, all but two specimens have acceptable surface condition; those two specimens both have a power of 1000W, and ED of $\sim 2.7 J/mm^2$. In all other cases, we can define a convex region which roughly captures where poor surface condition occurs. For $step > 0$ and *dot* scans, this region is centered at a power of 1000W, and ED of $3 J/mm^2$. For $step = 0$, the poor surface condition area is greatly expanded for either scan strategy, especially for *line*.

These convex regions are not perfect predictors of surface roughness, which is expected due to the highly stochastic nature of surface roughness. The exact borders of these regions are also poorly defined and, in some cases, overly reliant on individual specimens. There were practical issues when sampling regions with very poor surface condition: risk of machine damage and harming other results limited how many specimens could be used to explore the boundaries of this region. Thus, the boundary is sometimes overly affected by a single datapoint. Acknowledging this major limitation, Figure 31 shows a confusion matrix for these regions ability to predict surface roughness. True

negatives are most prevalent for the reasons stated above. The results constitute an F1-score of 83%, which is decent given the high variance in surface roughness that may cause many specimens to marginally cross the threshold.

The boundaries of the identified regions can be interpreted by considering traditional results for balling in AM: generally, balling occurs at high speed and power due to Plateau-Rayleigh instability [37]. Using the featurization of Energy Density (ED) and Power, this instead corresponds to high power, low ED. However, at too low of an ED, balling is present but meltpools are too small to result in significant surface roughness. Thus, there is a range of ED at each power where high surface roughness occurs, resulting in a roughly triangular region of “poor” results that grows with power. *Step* mitigates balling by creating multiple meltpools separated by distance, effectively acting as multiple beams at a lower speed. One interesting result is that *line* scans were better than *dot* scans for $step > 0$, but worse for $step = 0$. Comparing between $step = 0$ and $step > 0$ for the *line scan*, for $step > 0$ balling only occurred for two specimens at 1000W, the highest power tested, while at $step = 0$ it still occurred at just 250W, the lowest tested. Thus, at similar Energy Density, the threshold for balling at $step > 0$ was at least at a 4x greater power, equivalent to a 4x lower beam speed. By employing the quasi-beam strategy, a similar increase in print rate can be achieved while still avoiding balling.

4.4.3 Density Highly Dependent on Energy Density, Power

The final response surface was quite simple, with *Energy Density* and *Power* both having a positive relationship with density (Figure 33), and other factors showing less

significant effects. While it likely that this response could have been modelled without ML, BO still had utility in efficiently choosing new batches of specimens.

Energy Density was the dominant factor in increasing density, with a lesser increase with *Power*. The importance of ED can be understood as the result of lack of fusion occurring at lower energy densities. Density increases were greatest up to an ED of approximately 4 J/mm². Relative to the pycnometric density of 8.64 g/cm³, the observed Archimedes densities were somewhat lower. The expected density only exceeds 8.4 g/cm³, or 97% dense, near the maximum power and energy density tested. However, from microscopy it is clear the Archimedes density measurements are conservative. Figure 38 and Figure 39 shows specimens with an ED of 9.47 and 4.85 J/mm², respectively. In both it can be observed that the core of the specimen is nearly fully dense, with most pores and cavities concentrated towards the sides and bottom edge. On the bottom this is likely due to the architected break-off leaving some partially melted areas. On the sides, this is likely due to similarly partially melted regions on account of the high preheat creating a transitory boundary. Comparing between Figure 38 and Figure 39, the increase in density with energy density is mostly due to a decrease in these edge effects. By contrast, Figure 40 shows significant lack of fusion and large pores throughout the specimen. We summarize these results as follows: up to ~4 J/mm², there is significant increase in density due to transition from lack of fusion to fully dense cores. Above this, there are marginal gains due to more complete melting at the edges.

4.4.4 Statistically Significant Relationships Between Energy Density and Mass Magnetization

Statistically significant relationships were found between mass magnetization and *Energy Density/Step*, with approximately a 1% from the combined effect of both of these. This is in addition to the effect of increasing density and reflects a change in intrinsic material properties on a mass basis. This creates an interesting direction for future research. While the effect of Energy Density may have an effect due to more complete melting, the effect of *Step* has a less certain explanation.

4.4.5 Low Coercivity Driven by PBF-EB Thermal History

Coercivity was not found to be dependent on any factor, with H_c generally between 150-200 A/m but with outliers in both directions. This is an improvement on prior AM results for Permalloy printed by PBF-LB, which typically show >200 A/m even after significant post-processing [18, 40]. The lack of dependence on print parameters as well as the low value by AM standards is likely a result of Electron Beam Powder Bed Fusion being a hot process. The pre-heat to 850°C, and approximate 24 hr cooldown to room temperature (Figure 26) act as a heat treatment, increasing grain size and decreasing coercivity.

4.5 Conclusion

Utilizing high-throughput measurements, a stable process window was found with near fully dense cores and good surface condition. Advanced scan strategies could be included due the size of the dataset, and it was found that quasi-beam patterning as

represented by the factor of *step* had a decisive role in reducing Plateau-Rayleigh instability, decreasing the threshold for balling in beam speed by roughly a factor of 4. Density was successfully modelled by Gaussian Process Regression, which enabled the use of active learning to autonomously guide experiments. High-throughput magnetic characterization enabled relations to be observed for magnetic properties as well. It was found that mass magnetization increased by roughly 1% with increasing energy density and advanced scan strategies. While no trends were observed for coercivity, H_c was generally less than 200 A/m which represents an improvement on prior art. Additionally, other aspects of rapid experimentation were demonstrated, such as an architecture for “break-off” specimens.

CHAPTER 5. CLOSING

5.1 Overall Conclusions

In support of the characterization needs of automated laboratories for materials development, a high-throughput method for characterizing the magnetic properties of bulk specimens was developed. Its accuracy, repeatability, and throughput were shown to be sufficient for screening and exploration of broad feature spaces. This method was then demonstrated in practice as applied to the process development of the Electron Beam Powder Bed Fusion of Permalloy, along with other high-throughput methodologies. A stable process window was found, utilizing hundreds of density, surface roughness, and magnetic measurements. The large feature space allowed numerous relations to be discovered. For example, building on previous work, PBF-EB “quasi-beam” scanning techniques were shown to dramatically reduce melt pool instabilities that lead to balling. Magnetic saturation was also shown to improve with energy density, beyond what would be expected from increases to density alone.

5.2 Limitations and Future Work

5.2.1 *Magnetic Characterization*

A major advantage of the proposed instrument for magnetic characterization is its ability to make continuous measurements. The actual sampling rate, however, was limited by that of the thought-beam sensor. This averaged approximately 70 Hz. A future version could increase this significantly with dedicated sensors. While the time to measure a magnetic hysteresis loop will have diminishing returns relative to the current <20 seconds,

data rich measurements such as First-Order Reversal Curves (FORC) would benefit greatly from continued improvement.

Future improvements could improve accuracy and repeatability as well, such as with temperature monitoring and more detailed qualification and calibration. Future work could even use engineered magnet geometries to produce a more uniform field [41]. There is also a strong need for an improved method of mounting samples; the simple set screws used struggled with larger, misshaped AM specimens. This could likely be solved simply with an articulated clamped. While saturation magnetization measurements already show good accuracy and repeatability, coercivity measurements likely will remain imprecise compared to alternatives. Finally, there is a need for further qualification of size and shape effects. None of the pre-characterized specimens used for qualification were as large as the AM specimens printed in this study. Thus, the magnetization results for these large results may have an unknown bias and should be taken as primarily for self-comparison.

Another disadvantage of the proposed instrument is that it is limited to soft magnets due to the limited fields created by permanent magnets. At the cost of much of the current simplicity, using electromagnets instead of permanent magnets could enable the characterization of hard magnets as well. Another limitation of this instrument is that it is currently confined to DC measurements. In many applications AC measurements are of primary interest. Through rapid actuation it may be possible to achieve low frequencies, which would require careful accounting for the inertia of the flexure. If even 60 Hz could be reached, that would greatly extend the utility of this device.

One major extension that could significantly increase the capability of the instrument is to extend it to the characterization of 3D magnetization histories. Currently, this can only be done by specialized equipment. Exploiting the compact construction, the main axis of the two permanent magnets could be pivoted in two rotational degrees of freedom relative to the specimen to control complex magnetization histories. Benefitting further from the high rate of measurement possible, this could enable an instrument competing not just in cost and throughput but in the rare capability to characterize complex 3D histories.

5.2.2 *Electron Beam Powder Bed Fusion*

5.2.2.1 General AM methodologies

One method developed in this work were break-off specimens that could be easily removed from the build plate. An issue with this method is that it tended to leave significant defects and porosity at the point of break, which negative affected density measurements. A simple jig to allow the consistent grinding or sandblasting of the bottom face could mitigate this. Additionally, it was difficult to tailor the number of weakened layers for a wide range of energy densities with different melt pool depths, occasionally resulting in specimens not adhering to the build plate (or difficult to remove); future work may consider developing a model that can predict the number of break layers required.

Gaussian Process Regression (GPR), while successfully at modelling density, failed to capture surface roughness. There are many other ML approaches that may have been more successful, but a challenge for future work is how to appropriately choose models for any number of different responses.

5.2.2.2 Further Process Development for Permalloy

There were also flaws in the specific study of Permalloy. Lower energy densities were over-sampled, and the upper limit on power at 1000W was too low. This limit was motivated by inexperience with the open loop temperature control of the Freemelt ONE, but the current results indicate that greater densities and print rates could be achieved without balling at higher powers, by utilizing quasi-beam strategies explored. Another improvement could have been made in beam focus, estimated to have a width of $500\mu\text{m}$. This could have been reduced by approximately a factor of two with better calibration. The possible benefits of this should be explored, especially at lower energy densities where the better focus would have the greatest effect. Future work must also perform more extensive characterization of microstructures, to build on these preliminary screening results. The possible effect of *step* on magnetization is one such interesting direction requiring further direction.

APPENDIX A. HIGH-THROUGHPUT MEASUREMENT OF THE COEFFICIENT OF THERMAL EXPANSION OF AM SAMPLES

1. Introduction and Background

The coefficient of thermal expansion (CTE) measures the relative change in free length of a solid under changing temperature. In one dimension, this can be expressed as

$$\alpha = \frac{1}{L} \cdot \frac{dL}{dT} \quad (15)$$

where α is the CTE, L is the free length, and T is temperature. The CTE often stays nearly constant for large ranges of temperature, and thus often can be approximated by the following:

$$\alpha = \frac{\Delta L}{L\Delta T} \quad (16)$$

CTE is of broad engineering importance, and many materials have tailored CTE for specific engineering applications. α is typically expressed in terms of $\mu\epsilon/K$, microstrain per Kelvin. Low-expansion alloys such as Invar have near zero CTE at certain temperatures, which can minimize deformations due to temperature in scientific or industrial equipment. Other alloys are designed to match a particular CTE, such as Kovar which is designed to have a similar CTE to certain glasses. Additionally, CTE is coupled to many other phenomena, such as magnetic properties, and thus is an important measurement in materials research.

Dilatometry is the most common method for measuring the CTE, where the change in length is directly measured. This is broadly done in three different ways: contact, interferometric, or optical. These methods generally have low-throughput due to the need to individually cycle a furnace for each sample, and further require samples to be heavily pre-processed to achieve necessary form and finish. Recently, Digital Image Correlation (DIC) has been utilized for high-throughput CTE measurements [11]. The advantages are the possibility of parallel measurements, within a single furnace cycle. However, this still necessitates preprocessing such that the sample can be imaged by DIC.

2. Theory and Design

We propose an optical dilatometry technique that does not require furnace cycling through use of high repeatable length measurements. Figure 41 shows the general architecture of the required instrument. A sample is placed on a rotating platform that can be heated to act as a hot plate. A 2D Through-beam Sensor records the width of the sample, perpendicular to the axis of rotation. Only RZ rotation of the sample will affect this measurement, eliminating the need for precise position in the other degrees of freedom (DOF).

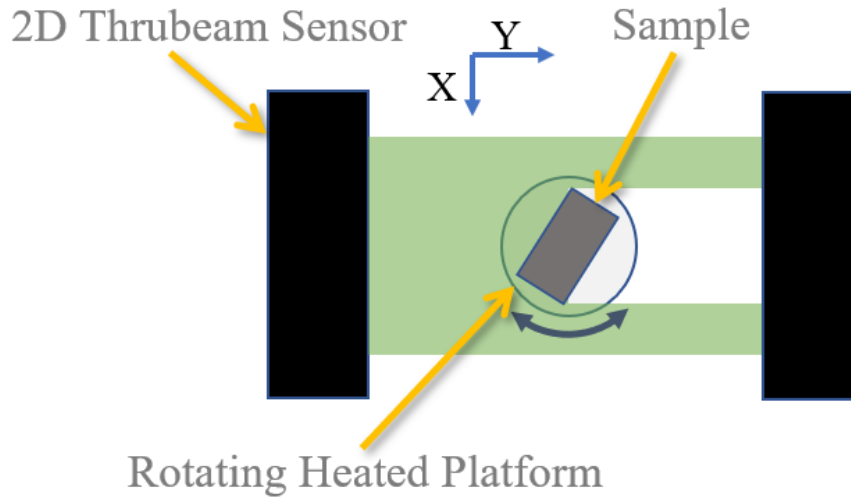


Figure 41: Arrangement for repeatable length measurements of samples

By oscillating the heated platform there will be a sinusoidal response in the measured width, which from simple trigonometry we model as:

$$L(\theta) = L_0 \cos(\theta + \delta) + R \quad (17)$$

where L is the measured length, L_0 is the maximum width, and R accounts for smooth corners. By fitting this sinusoid, $L_0(T)$ can be calculated, where T is the temperature of build plate. With a relatively flat sample, T will closely control the temperature of the sample as well. If L_0 is sufficiently repeatable, then measurements at different temperature do not need to be done in series. Instead, all measurements at a single T_0 can be done in series, and then all measurements at some T_1 done in series. Thus, all but one heating cycle can be avoided.

L_0 is repeatable to within approximately $0.5\mu m$. The given repeatability of the through-beam sensor by the manufacturer is $\pm 0.1\mu m$; the worse result is because of additional error compounded establishing the datums, and from the thin, uneven edges

being fit to. For a 20mm sample and $\Delta T = 20^\circ C$, the theoretical precision in α would be $0.5 \mu\epsilon/K$ based on this precision. A typical value for a metal alloy is $\alpha = 10 - 20 \mu\epsilon/K$, so this is reasonably discerning.

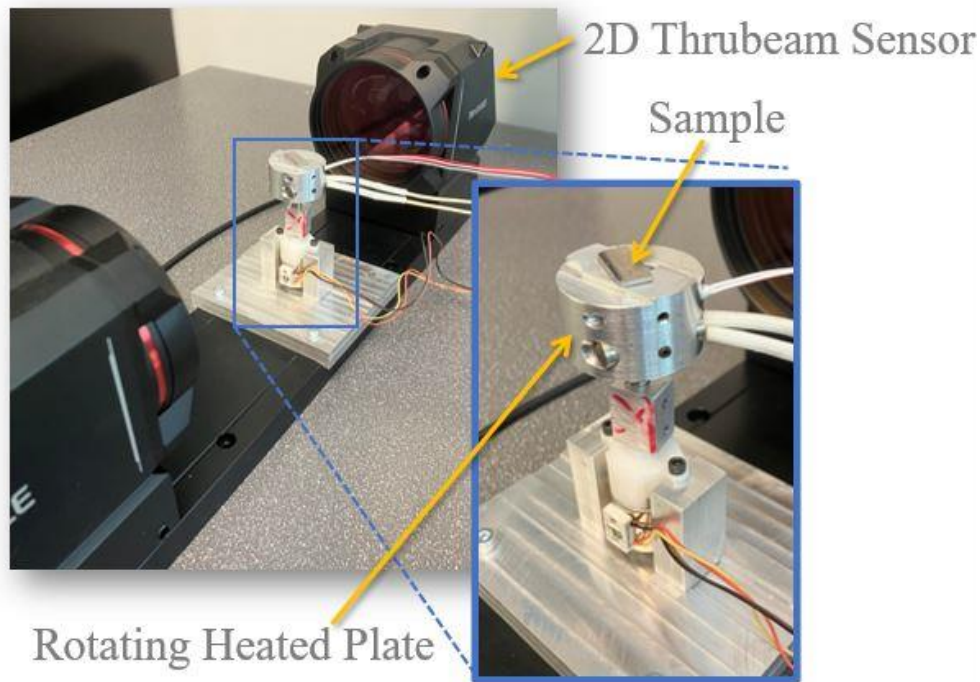


Figure 42: Prototype of the proposed instrument for characterizing CTE

A prototype of the proposed instrument is shown in Figure 42. The Keyence TM-x5065 is used as the through-beam sensor. The heated plate is made of aluminum and rotated by a stepper motor. Figure 43 shows the varying of width for a series of consecutive oscillations. Each individual oscillation is identified based on the appearance of local peaks, and a sinusoid is fit to all measured widths within $100\mu m$ of that peak. The samples are not precisely aligned on the plates; windowing in this manner ensures a consistent and comparable fit.

3. Results and Discussion

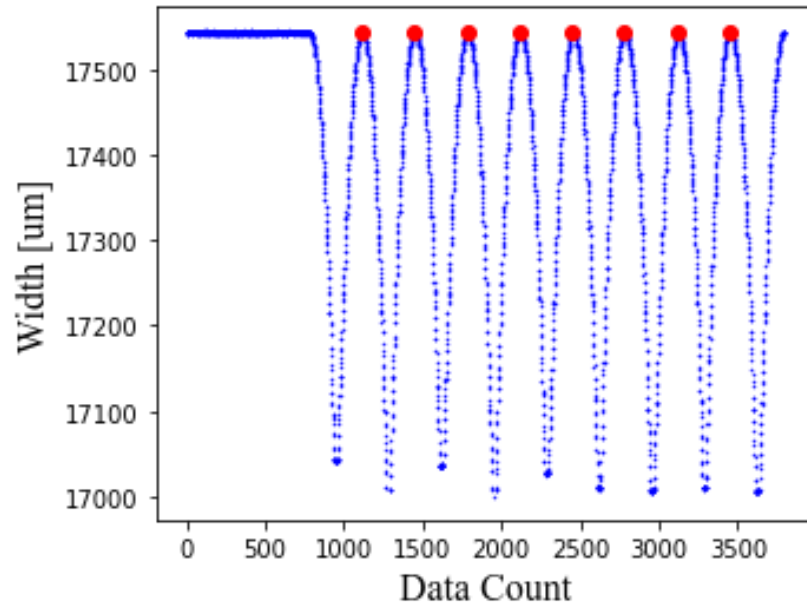


Figure 43: Measured width by the 2D through-beam sensor during a series of oscillations. These peaks can be easily recognized computationally, as indicated by the red dots.

A sample of additively manufactured Kovar is measured first at room temperature (20°C), and then at an elevated temperature of 75°C. 8 oscillations are performed at each temperature and fit individually. These results are shown Figure 44. It can be seen the individual oscillations slightly disagree in phase (δ). This is because the sample may shift slightly between oscillations, as the direction change creates a sudden rotational acceleration. This necessitates individually fitting each oscillation.

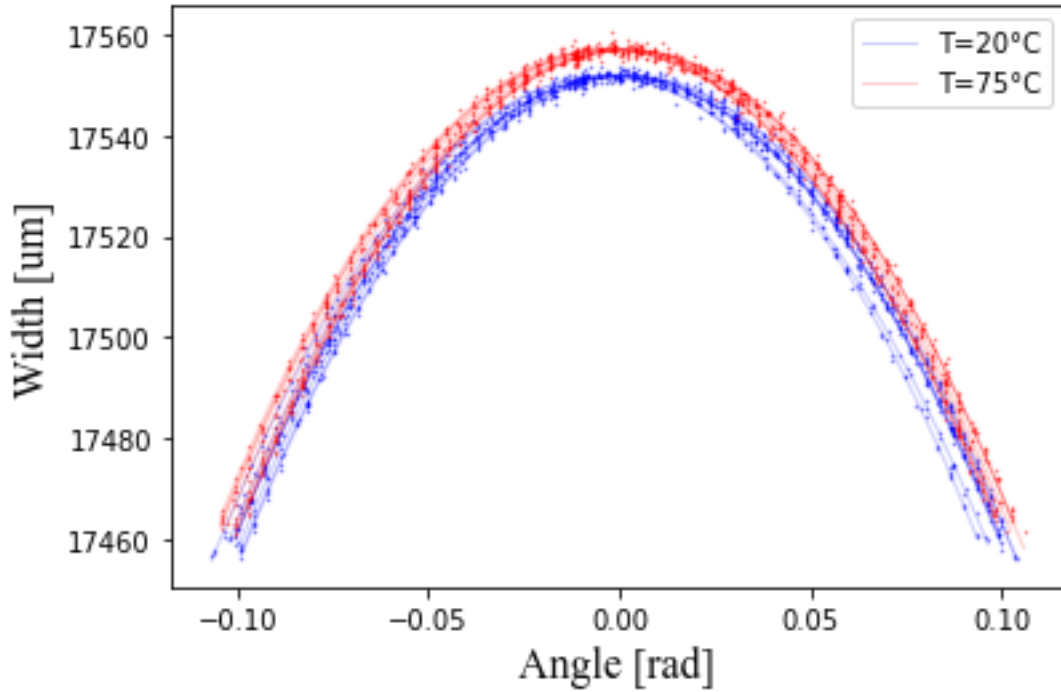


Figure 44: Results of fitting each oscillation at room temperature and elevated temperature. A clear and consistent increase in measured width can be observed.

Table 11: Fit results for Kovar specimen

Temperature [$^{\circ}C$]	\bar{L}_0 [μm]	σ_{L_0} [μm]
20	17551.91	0.07
75	17557.16	0.13

From the results in Table 11, it can be calculated that $\alpha = 5.44\mu\epsilon/K$. The wrought value for Kovar at room temperature is $5.8\mu\epsilon/K$, so this is reasonable agreement.

4. Conclusion

This initial prototype demonstrates the potential of this instrument to achieve high-throughput CTE measurements by eliminating the need for pre-processing or furnace cycling. One major challenge is that the temperature of the sample will not be equal to the known temperature of the heated plate, but rather will reflect an equilibrium

between conduction and convection. This can create significant error when the surface condition of the sample is poor. One possible solution could be using a thermally conductive fluid intermediate, or partially enclosed furnace that still permits the relevant measurements to be made. Future work must perform further qualification of this instrument, and better understand and mitigate these possible sources of error.

APPENDIX B. DETAILS OF CALCULATION OF MAGNETIC FIELD FROM PERMANENT MAGNET POSITIONS

An Ansys 2022 R1 Magnetostatic Simulation was used to calculate the field along the axis of single permanent magnet. For the N52 permanent magnet, the 2nd quadrant demagnetization curve was used with remnant magnetic flux density B_r of 1.44T. The geometry was idealized as a $\phi 25.4 \times 25.4$ mm cylinder. The magnet was modelled as a half-cylinder with a symmetry plane, surrounded by air. A 1mm mesh was used in region emanating from one face of the permanent magnet to allow for granular probing of this region, which bounded convergence. The results of this Finite Element Method (FEM) simulation are shown in Figure 45.

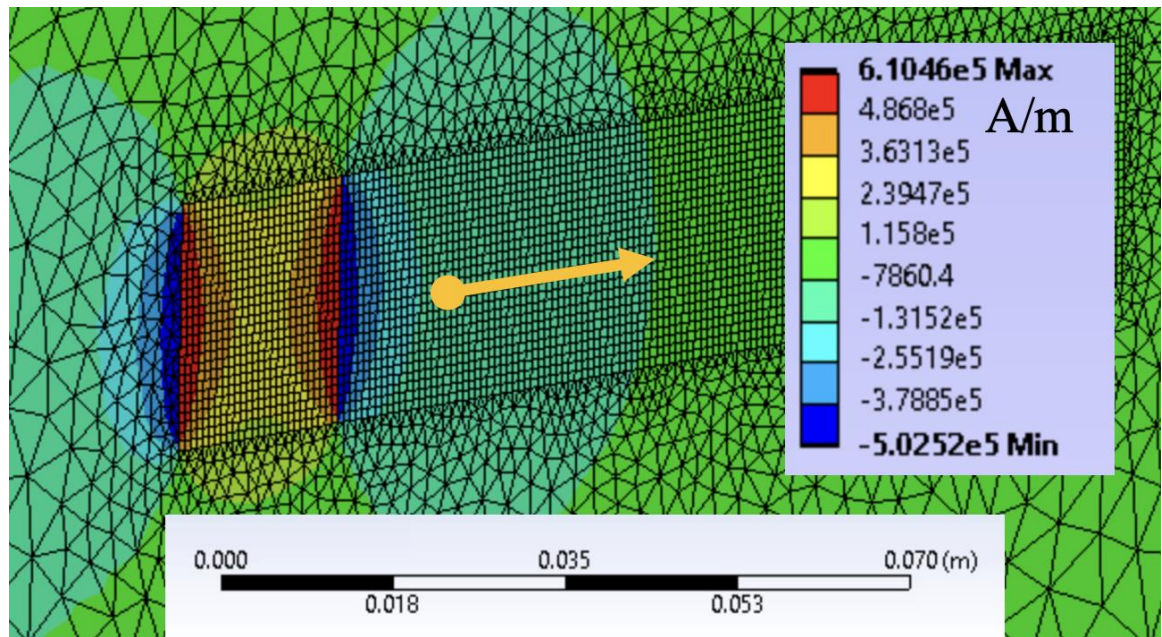


Figure 45: Finite Element Method Study of magnetic field created by N52 permanent magnet. Directional magnetic field is measured along the indicated direction.

The results along the center axis were probed to measured magnetic field H as a function of distance to the face of the magnet. To calculate the field from two permanent magnets, these results are superimposed upon each other (accounting for orientation). This means the FEM model only had to be run once. While the permanent magnets will affect each other's magnetization, the minimum distance between the two (~50mm) and hardness of the magnets results in this effect being small.

REFERENCES

1. National Academies of Sciences, E. and Medicine, *frontiers of materials research: A decadal survey*. 2019: National Academies Press.
2. Boyce, B., et al., *Machine learning for materials science: Barriers to broader adoption*. Matter, 2023. **6**(5): p. 1320-1323.
3. Boyce, B.L. and M.D. Uchic, *Progress toward autonomous experimental systems for alloy development*. MRS Bulletin, 2019. **44**(4): p. 273-280.
4. Frazier, W.E., *Metal additive manufacturing: a review*. Journal of Materials Engineering and performance, 2014. **23**: p. 1917-1928.
5. DebRoy, T., et al., *Additive manufacturing of metallic components—process, structure and properties*. Progress in Materials Science, 2018. **92**: p. 112-224.
6. Robertson, I.M., et al., *Towards an integrated materials characterization toolbox*. Journal of Materials Research, 2011. **26**(11): p. 1341-1383.
7. DeCost, B.L., et al., *High throughput quantitative metallography for complex microstructures using deep learning: A case study in ultrahigh carbon steel*. Microscopy and Microanalysis, 2019. **25**(1): p. 21-29.
8. Nyshadham, C., et al., *Machine-learned multi-system surrogate models for materials prediction*. npj Computational Materials, 2019. **5**(1): p. 51.
9. Salzbrenner, B.C., et al., *High-throughput stochastic tensile performance of additively manufactured stainless steel*. Journal of Materials Processing Technology, 2017. **241**: p. 1-12.
10. Courtright, Z.S., et al., *Critical comparison of spherical microindentation, small punch test, and uniaxial tensile testing for selective laser melted Inconel 718*. Applied Sciences, 2021. **11**(3): p. 1061.
11. Dong, Y., Z. Zhang, and B. Pan, *High-throughput, high-accuracy determination of coefficient of thermal expansion of carbon fibre–epoxy composites using digital image correlation*. Strain, 2018. **54**(1): p. e12259.
12. Yuan, J., et al., *Recent advances in high-throughput superconductivity research*. Superconductor Science and Technology, 2019. **32**(12): p. 123001.
13. Cong, P., et al., *High-throughput synthesis and screening of combinatorial heterogeneous catalyst libraries*. Angewandte Chemie International Edition, 1999. **38**(4): p. 483-488.

14. Zhou, T., et al., *Origin of high-frequency magnetic loss of Y3Fe5O12 single crystal thin films prepared with high-throughput screening by magnetron sputtering*. Vacuum, 2023. **207**: p. 111644.
15. Geng, J., et al., *Bulk combinatorial synthesis and high throughput characterization for rapid assessment of magnetic materials: Application of laser engineered net shaping (lens™)*. Jom, 2016. **68**: p. 1972-1977.
16. Lamichhane, T.N., et al., *Additive manufacturing of soft magnets for electrical machines—A review*. Materials Today Physics, 2020. **15**: p. 100255.
17. Chikazumi, S., *Physics of ferromagnetism*. 1997: Oxford university press.
18. Mikler, C., et al., *Laser additive manufacturing of magnetic materials*. Jom, 2017. **69**: p. 532-543.
19. Rybachuk, V. and B. Filyushyn, *Coercimeters for magnetic nondestructive testing of materials and products*. Materials Science, 1997. **33**(5): p. 651-654.
20. Flanders, P., *An alternating-gradient magnetometer*. Journal of Applied Physics, 1988. **63**(8): p. 3940-3945.
21. Körner, C., *Additive manufacturing of metallic components by selective electron beam melting—a review*. International Materials Reviews, 2016. **61**(5): p. 361-377.
22. Herzer, G., *Nanocrystalline soft magnetic alloys*. Handbook of magnetic materials, 1997. **10**: p. 415-462.
23. Guthrie, W.F., *NIST/SEMATECH e-Handbook of Statistical Methods (NIST Handbook 151)*. National Institute of Standards and Technology: Gaithersburg, MD, USA, 2020.
24. Wang, C., et al., *Machine learning in additive manufacturing: State-of-the-art and perspectives*. Additive Manufacturing, 2020. **36**: p. 101538.
25. Agrawal, A. and A. Choudhary, *Deep materials informatics: Applications of deep learning in materials science*. Mrs Communications, 2019. **9**(3): p. 779-792.
26. Noack, M.M., et al., *Autonomous materials discovery driven by Gaussian process regression with inhomogeneous measurement noise and anisotropic kernels*. Scientific reports, 2020. **10**(1): p. 17663.
27. Qi, X., et al., *Applying neural-network-based machine learning to additive manufacturing: current applications, challenges, and future perspectives*. Engineering, 2019. **5**(4): p. 721-729.

28. Herbol, H.C., M. Poloczek, and P. Clancy, *Cost-effective materials discovery: Bayesian optimization across multiple information sources*. *Materials Horizons*, 2020. **7**(8): p. 2113-2123.
29. Waide, P. and C.U. Brunner, *Energy-efficiency policy opportunities for electric motor-driven systems*. 2011.
30. Song, Y., et al., *Negative thermal expansion in magnetic materials*. *Progress in Materials Science*, 2021. **121**: p. 100835.
31. *HIPERCO 50*. [cited 2023 7/25]; Available from: <https://www.carpentertechnology.com/alloy-finder/hiperco-50>.
32. *HYMU 80*. [cited 2023 7/25]; Available from: <https://www.carpentertechnology.com/alloy-finder/hymu-80>.
33. *Permalloy 80*. [cited 2023 7/4]; Available from: <https://espimetals.com/index.php/technical-data/175-Permalloy%2080>.
34. Tapia, G. and A. Elwany, *A review on process monitoring and control in metal-based additive manufacturing*. *Journal of Manufacturing Science and Engineering*, 2014. **136**(6): p. 060801.
35. Babuska, T.F., et al., *Achieving high strength and ductility in traditionally brittle soft magnetic intermetallics via additive manufacturing*. *Acta Materialia*, 2019. **180**: p. 149-157.
36. Plotkowski, A., et al., *A stochastic scan strategy for grain structure control in complex geometries using electron beam powder bed fusion*. *Additive Manufacturing*, 2021. **46**: p. 102092.
37. Yang, J., et al., *Electron beam-based additive manufacturing of Fe₉₃.5Si₆.5 (wt.%) soft magnetic material with controllable magnetic performance*. *Scripta Materialia*, 2022. **210**: p. 114460.
38. Firdosy, S.A., et al., *Laser-Deposited Soft Magnetic Fe–Ni–Mo Alloy: A Processing—Microstructure Study*. *Metallography, Microstructure, and Analysis*, 2022. **11**(1): p. 108-118.
39. *METAL POWDER BY SANDVIK*. Available from: <https://www.metalpowder.sandvik/en/>.
40. Mohamed, A.E.-M.A., et al., *Magnetic shielding promotion via the control of magnetic anisotropy and thermal Post processing in laser powder bed fusion processed NiFeMo-based soft magnet*. *Additive Manufacturing*, 2020. **32**: p. 101079.

41. Galchenko, V.Y., A. Yakimov, and D. Ostapushchenko, *Solution of the inverse problem of creating a uniform magnetic field in coercimeters with partially closed magnetic systems*. Russian Journal of Nondestructive Testing, 2011. **47**(5): p. 295.